Plasma instability in the presence of negative ions

J. A. Johnson III
Department of Physics, The City College, City University of New York, New York, New York 10031

Raghu Ramaiah*
Department of Physics, Rutgers University, New Brunswick, New Jersey 08903
(Received 23 December 1986)

Ion density fluctuations are studied in a diffusion-controlled argon plasma containing, as a dilutant, two electron-attaching species, carbon dioxide, and sulfur hexafluoride. A glow discharge tube is used in this experiment; electrical probes and digital spectral analysis are our principal diagnostic and analytical tools. It is found that the system becomes increasingly unstable as the concentration of the electron-attaching species is increased. Nonlinear mode-mode couplings have been identified and the coupling coefficients for these interactions have been computed. Turbulent fluctuations are observed to have pronounced three dimensionality with distinct axial and azimuthal behaviors. The power spectra of these fluctuations are composed of many discrete modes and follow a $P(w) \propto w^{-n}$ trend with $3 < n < 5$. The importance of changes in the total discharge pressure is dependent on the electron-attachment cross section of the dilutant species. From these results we show that the ionization instability is probably responsible for the observed phenomenon.

I. INTRODUCTION

Weakly ionized glow discharges are known to be susceptible to the development of instabilities, typically manifest in the form of ionization waves and as a constriction of the plasma. Specifically, the ionization instability, which results from a temporal amplification of an imbalance between charged-particle production and loss processes during disturbance in the plasma properties, excites various modes of the system. In the presence of nonlinear interactions between the modes, the transition to a turbulent system takes place fairly rapidly. The most complete previous treatment of high-pressure convectively cooled gas discharges in electronegative gases is strictly limited to a plasma dominated by volume behavior; the transport processes are neglected. Several experimental and theoretical investigations have been conducted in electropositive gas discharges.[1-11] By comparison, only a few essentially qualitative reports can be found on electronegative discharge instabilities.[11-21] Indeed, quantitative treatments of nonlinear phenomena associated with instabilities in electronegative gases are virtually nonexistent.

This paper presents an experimental investigation of the ionization instability of electronegative gas mixtures in a diffusion-controlled, low-pressure discharge plasma. Gas mixtures of Ar with SF_6 and of Ar with CO_2 will be used in our study. The ion density fluctuations in the positive column of the electronegative gas discharge are monitored by a unique array of Langmuir probes which allows measurements to be made in the azimuthal and axial planes. The probe fluctuations are digitized and data analyses are performed by standard spectral techniques. Specifically, we wish to study the importance of the negative-ion concentration and the total gas-mixture pressure as parameters, in the sense that the Reynolds number is used in conventional hydrodynamics, to characterize the instability and the turbulence of the system. We wish to determine the role which nonlinear mode-mode coupling plays in the development of turbulence. In this connection quantitative estimates of the coupling coefficients for these interactions are obtained. Finally, a qualitative physical model is presented which lends insight into the origin of this instability.

In Sec. II a review of the previous theoretical and experimental works on instabilities and electronegative gases is given. Section III describes the experimental setup and methods, including the design of the discharge tube, the operations of the various diagnostic and the data acquisition system, the methods of data analysis and the various calibration procedures. Section IV presents the experimental results including samples of the ion density fluctuation, autopower spectrum, cross-power spectrum, dispersion relations, correlation function, spectral indexes, and the results of the bispectral analysis. In Sec. V the experimental results are discussed and a physical model is presented. Conclusions and suggestions follow in Sec. VI.

II. BACKGROUND

A. Mechanism of the discharge

For an active discharge in a rare gas at low pressure, there must be a source of electrons, i.e., a cathode, be it either a cold metal plate, which emits secondary electrons due to ion bombardment, impact of metastable gas atoms, or sufficiently energetic ultraviolet radiation,[14,22] or a hot thermionically emitting surface. Conditions adjacent to the cathode must be such as to give a sufficient yield of electrons; in the case of ion bombardment, this yield determines the electric potential drop immediately in front of the cathode. Strong fields at the cathode result in the electrons being accelerated to energies greater than the op-

timum for causing ionization. There are, therefore, regions in which the initial electrons are scattered and lose energy until the motion is randomized and an optimum situation is achieved. When this is reached it is possible for there to be a set of equilibrations between the energy input from the longitudinal field and the loss of energy due to inelastic collisions with the gas atoms, between the momentum gained from the electric field and that lost in elastic and inelastic collisions, and finally between the particle generation process of ionization of the gas atoms by electron impact and the loss process associated with the motion of particles to the walls. The loss process arises because there are radial electric fields caused by the charged particles which lead to their motion in a radial direction; this motion may be treated as free flight at very low pressures or diffusive at moderate pressures. At high pressures, when the various fields are low, recombination in the volume is an important process.

The equilibrium situation then can be axially uniform; it is such a region which is usually referred to as the positive column of an active discharge. Because the number density of charged particles is maintained by ionization, their motion must be collisional. Since ionization from the ground state requires more energy transfer than any excitation process, there will be an appreciable density of excited particles and consequently radiation will be emitted corresponding to the allowed transitions between excited states of the gas atoms; the spectra being characteristic of the gas used. The fact that the charged particles are generated in the volume and are lost at the walls means that there must be radial variations in the charged-particle density, so that the discharge is not radially uniform. On the other hand, if the radial fields are not so strong as to cause charge separation throughout the volume or (equivalently) if the discharge is Debye lengths in radius, the densities of positively and negatively charged particles will be almost equal.

The longitudinal field along the positive column is small and uniform. The Poisson equation states that

$$(dE_z/dz)=e(n^+-n^-)/\epsilon_0 .$$

E_z was found experimentally[14,22] to be independent of z, which is further proof of the macroscopic neutrality of the positive column. Typical values of E_z range from 0.5 to 20.0 V/cm.

The theories of the positive column[1,14] apply only to certain approximate ranges of pressure, radius, and current, i.e., $p=10^{-4}$ to 10 mm Hg, $R=1$ to 10 cm, $i=10^{-4}$ to 1 A. At lower currents, the rate of ionization is too small to maintain the plasma properly neutral; at higher currents gas heating becomes appreciable.

All theories of the column have certain basic assumptions in common. These are a charge concentration given by $N^+=N_e=N$, a Maxwellian electron energy distribution, an electron temperature which is constant across the discharge, i.e., $T_e\neq f(r)$, electron mobility given by Langevin's equations, and the rate of ion production which is proportional to N_e. The discharge current and the tube radius are regarded as given.

Schottky's diffusion theory,[1,14,22] which applies at medium pressures (10^{-1} to 10 mm Hg) is of special relevance to this work. Here the loss of ions and electrons is due almost entirely to ambipolar diffusion, volume recombination being neglected. The main results of this theory are

$$N_r=N_0J_0(2.405r/R) ,$$

$$Z=(apm4/e\sqrt{\pi})(2kT_e/m)^{3/2}\times[1+(eV_i/2kT_e)]\exp(-eV_i/kT_e) ,$$

and

$$[1/(eV_i/RT_e)]^{1/2}\exp(-eV_i/kT_e)=1.16\times10^7(CpR)^2 ,$$

where N_r is the radial concentration, Z is the ionization rate, and C is a constant for the gas. These results have been confirmed by various experiments in the past.[3,14,22-24]

B. Instability and turbulence

At present the term turbulence is understood to mean the motion of a plasma in which a large number of collective degrees of freedom are excited. Thus when applying the term "turbulence" to a plasma, it is used in a broader sense than conventional hydrodynamics. If hydrodynamic turbulence represents a system made up of a large number of mutually interacting eddies,[25,26] then in a plasma we have together with the eddies (or instead of them), also, the possible excitation of a great variety of oscillations. Depending on the degree of freedom which is excited, the character of the interaction between the excitations may vary considerably. Due to the interaction between particles, the oscillatory motion of a single particle is spread over space and waves are generated. These waves are associated with the simultaneous variation of a number of quantities, all of which depend on one another; oscillating electromagnetic fields excite periodic currents and currents interacting with the magnetic field gives rise to a Lorentz force with leads to motion; the periodically varying velocity gives rise to pressure oscillations, which in turn produce density variations. Thus waves in a plasma are simultaneously electromagnetic and hydrodynamic even though, in particular cases, a certain aspect may dominate. In general, these waves are complex with features leading to instability.

Of particular interest to us are instabilities that arise in partially ionized plasmas. The recombination instability[27-29] is caused by an increase in the number of heavy charged particles at increasing electric fields and temperatures, causing in turn a decrease in mobility on account of recombination attachment and ionization processes (e.g., in an oxygen discharge). The recombination instability may be considered as a prototype of a more general class of instabilities which may occur in fluids undergoing density changes through volumetric processes. Specifically, molecular dissociation, chemical reactions, ionization, scattering into a loss cone in velocity space or thermonuclear reactions are all classified generically as volumetric instabilities.

The attachment instabilities[4,13,30] are further examples of volumetric instabilities. The ionization-recombination ion sound instability[31] is due to a coupling of the ioniza-

tion rate to density fluctuations in a partially ionized gas which are associated with ion-acoustic oscillations which may grow. The energy source of the instability is the thermal energy of the electron gas. It may be stabilized by collisional damping and other mechanisms. A more important example is the ionization instability[32,33] as it is the most common instability in a discharge.[4,13] In a partially ionized plasma the ionization rate increases strongly with electron temperature (as discussed above), so that small temperature fluctuations lead to large perturbations in the electron density. The ohmic heating due to an imposed electric current, which represents the energy source of the instability, and electron temperature are enhanced in regions of high electron density. Local perturbation of the electron density becomes unstable due to the corresponding fluctuation in the ionization rate. Heat losses by radiation and collision with heavy particles may damp the instabilities. An externally imposed magnetic field helps in reducing these losses. The presence of negative ions can lead to a build up ionization oscillation in a weakly ionized plasma and thus to a new type of ionization instability.[4,17,30]

Grabec[32,34] and others[13,35–40] have associated these ionization instabilities with the appearance of ionization waves in the positive column of a glow discharge. The waves are accompanied by variations in ionization rate, charge density, electron temperature, and electric field intensity. In Grabec's work, nonlinear equations describing the ionization waves are derived from the hydrodynamic equations for the plasma, from the Poisson equation, and from the ionization rate equation. The complete set of equations was then solved numerically and all the essential properties of ionization waves were recovered. Furthermore, it was shown that the collisions of ionization waves were of fundamental importance in turbulent positive columns. Specifically, a suggestion is made that nonlinear phenomena, notably harmonic generation and mode-mode coupling, play a significant role in the development of turbulence.

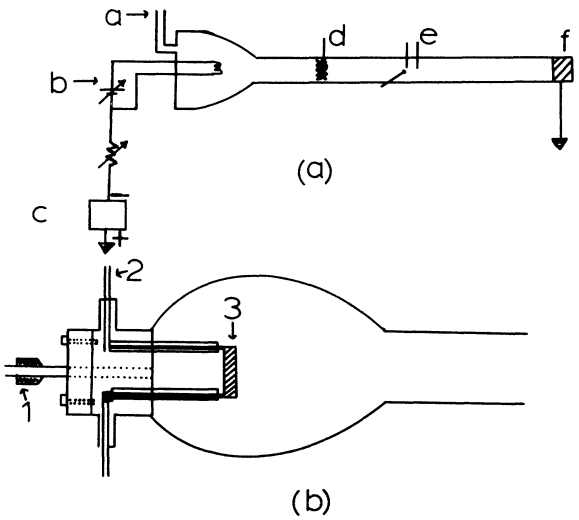

FIG. 1. (a) Schematic of the experimental setup. *a*, Gas input and exhaust; *b*, filament power supply; *c*, constant current 2 kV (dc) power supply; *d*, grid exciter; *e*, Langmuir probe array; *f*, grounded water cooled anode. (b) Detail of the cathode section. 1, Gas input and exhaust; 2, filament and cathode electrodes; 3, filament.

As a rule, turbulence develops as a result of an instability of an initial laminar state. In order to characterize this transition from the laminar to the turbulent state, it is convenient to examine the behavior of the system while changing some parameter, R, the increase of which results in the loss of stability. (In conventional hydrodynamics such a parameter is the Reynolds number.) In the quasilinear approximation,[25,26] one monitors the evolution of R with respect to some critical value R_1. When R only slightly exceeds R_1, the amplitude of the waves arising from the induced excitations can be determined by expanding solutions for laminar flow with respect to $(R-R_1)$, i.e., a small amplitude expansion (first used by Stuart[25]). In spite of the somewhat satisfactory results[12,13] for $R-R_1 \ll R_1$, this quasilinear method seems to be suitable only for the description of states which are so weakly excited that (strictly speaking) they ought not to be called turbulent, since the most important property of turbulence (the nonlinear interactions between the oscillations) is not yet apparent.[10,34]

C. Negative-ion effects

Discharges in gas mixtures containing molecular species which readily yield negative ions often exhibit behavior which is markedly different from discharges in other gases.[13–20] The fact that negative-ion processes occurring in such discharges are the cause of the observed behavior has been appreciated for many years. A comprehensive summary of these effects observed before 1960 was compiled by Francis.[14] These are (a) an apparent increase in gas density, (b) creation or concentration of regions of negative space charge, and (c) a change in the distribution of negative carriers.

A survey was made of experiments on constricted and unstable positive columns in electronegative gases at low pressure.[15] Here attention is mainly focused on the constriction of the column and the ensuing instability. The main results are (a) mobile and stable forms can exist in the discharge at various positions along the axis, (b) probe measurement show that a large number of negative ions exist inside the core, (c) comparing the results with previous workers for constriction and instability in inert and molecular gases without negative ions, it was found that negative ions produce similar effects at much lower pressures that can be observed in their absence, (d) one part of the column may be constricted but stable while a neighboring part may be simultaneously more constricted and unstable, with no sharp demarcation between the sections, and (e) moving striation (ionization waves) were always present in constricted columns of electronegative discharges.

These early attempts to explain the role of negative ions in the instabilities of these columns were largely empirical. The availability of reliable cross-section data for attachment cross sections[13,21,41–48] involving common molecular species now permits the detailed theoretical analysis of

negative-ion processes and their influence on steady-state plasma properties of many discharges. An analytical treatment of the local low-frequency stability of a weakly ionized molecular system has been performed.[30] This analysis was extended to include negative-ion processes.[13,49] The main results of the works just cited are (a) attachment and detachment reactions can exert a profound influence on discharge operating conditions, (b) clustering of negative ions occurs with parent molecules (viz., the density of such negative clusters can become very large, having a significant influence on discharge behavior), (c) when the electron negative-ion densities are comparable, an attachment rate which increases with electron temperature can cause a mode of ionization instability; the attachment-induced ionization instability, (d) the ultimate manifestation of this mode of ionization instability is in the form of a striated plasma, and (e) addition of a small concentration of detaching species to reduce the concentration of negative ions results in the elimination of the striations.

The most important conclusion of the above work from our standpoint is that the modes of instability associated with electron production and loss (ionization instability) and with negative-ion production and loss (negative-ion instability) can occur for easily attainable discharge conditions. Electron-attachment-induced ionization instability[13,30] has the largest growth rate of the two modes and will therefore dominate plasma temporal behavior, ultimately leading to a striated plasma. It should be mentioned that the causes of charged-particle production instability leading to the commonly observed striated discharge are, in general, extraordinarily complex[13,30,32,35–39] and vary greatly as gas species and plasma operating conditions are changed.[13,38] Therefore it is important to remember that the results and conclusions of the above work are not applicable for *all* situations, but they are limited to electrically excited molecular gas discharges which are dominated by volume phenomena, with transport processes being essentially neglected.

More specifically, papers[16,17] by Suganomata *et al.* have reported instabilities in a discharge of SF_6. The discharge was initiated in pure SF_6, $p=150$ mTorr, $I=0.9$ mA, and $V=2.2$ kV. In addition, they used ring electrodes which limited their observation to fluctuations below 5 kHz. Definite solitonlike structures were observed in all cases, implying the occurrence of some nonlinear phenomenon.

D. Preview

As indicated above, the positive column in a gas discharge is rarely in a quiet state. The most common instability in this system, which leads to the development of ionization waves, is the ionization instability. Several papers and review articles have appeared regularly attesting to the widespread interest in this phenomena.[6,9,32,38,39] The chief concern of these articles has been the study of ionization waves in electropositive gases. At the present time, available studies of glow discharges in electronegative gases are entirely inadequate with regard to the treatment of the dynamics of instabilities. In particular, quantitative treatment of nonlinear phenomena in such systems are almost nonexistent[13,16,17] in spite of the importance of such effects. Subsequent advances in digital techniques[49–57] data acquisition, digitization, and computer processing hardware have made detailed quantitative studies possible.

Consider two electronegative gases SF_6 and CO_2 which have been studied in other contexts in the past.[13,41,42] There are two modes of formation of the following negative ions which are used.

(i) SF_6: *Resonance capture* (Refs. 41,45,47,58)

$$e^- + SF_6 \rightarrow (SF_6^-)^* \begin{matrix} \nearrow SF_6^- \\ \searrow SF_5^- + F \end{matrix} .$$

It appears that some of the excited ions $(SF_6)^*$ dissociate whereas others do not, with approximately equal likelihood. The overall cross section for this process is the highest among all electron-attaching species.

(ii) Co_2: *Dissociative attachment* (Refs. 13,21,41)

$$e^- + CO_2 \rightarrow CO + O^- .$$

The attachement cross section for this process exhibits two peaks at 4 and 8 eV. The cross section is considerably lower than the above case for SF_6.

As discussed in Sec. II B above, a general parameter R may be employed to describe the behavior in an unstable system. We will determine that for a treatment of instabilities in electronegative gases, R can be the concentration of the electronegative component or the total gas pressure. The presence of mode-mode coupling, as this parameter R is varied, would be made unambiguously evident by the use of bispectral analysis.[53,54] In addition, values of coupling coefficients for these interactions can be obtained. Thus a complete linear and nonlinear analysis performed on the plasma fluctuations as the parameter R is varied can be used to determine the extent and nature of influence of negative ions on plasma stability.

III. EXPERIMENT

The glow discharge is obtained in a Pyrex glass tube of length 80 cm and an inner diameter of 2.5 cm. The discharge is established in mixtures of Ar with SF_6 and CO_2 and the total mixture pressures are varied in order to study the effect of negative ions on ionization instability. Thermionically emitted electrons assisted the discharge process; the positive column was obtained a few centimeters from the cathode.

Figure 1(a) shows the experimental setup. The main test section is located 40 cm from the cathode and consists of an array of Langmuir probes. These probes, operated under ion-saturated conditions, are the major ion diagnostic. In addition, one of these probes is used to monitor the plasma electron temperature and density at the probe site. Probe signals are digitized using an analog-to-digital converter (Biomation 8100) and then stored on a floppy disc system (Techtran 951). The stored data were subsequently transferred to a DEC-PDP 10 for data processing and analysis. A grid 2 cm in diameter and made of fine mesh steel wire was inserted in the positive column 12 cm from the test section. Pulses (80 V,

0.1 ms) were applied to the grid at various repetition rates (0.2–7.0 kHz) for some of the runs. The primary effect of the grid was to ensure that a source of instability was present at the probe site.

A. Discharge tube setup

The discharge tube consists of the following sections as shown in Fig. 1(b).

(a) The *cathode section* is 20 cm in length, with a Varian glass-metal joint at one end through which the filament electrodes are inserted into the cathode region. The filament is heated by an ac power supply (Varian Inc.) which is capable of withstanding a high dc voltage surge. Typical filament currents are 5 A. The cathode, driven by a high-voltage constant-current power supply (Voltronics Inc.), is connected via a ballast resistor [Fig. 1(a)] to one of the filament electrodes. Typical discharge current and voltages are 100 mA and 500 V. The gas input and exhaust are conducted through a vacuum-quick couple. Typical operating pressures are 100 mTorr. The other end of the cathode section terminates in a O-ring joint. The cathode section is connected to other sections via ring clamps which provide vacuum-tight connections, satisfactory for absolute pressure as low as 10^{-6} Torr.

(b) The *exciter section,* as shown in Fig. 1(a), consists of a hollow brass cylinder of length 3 cm and inner diameter of 2.5 cm, with connecting flanges. The dimensions of these flanges are exactly the same as those of the ring clamps, so that a good vacuum-tight seal to other sections is ensured. The exciter grid is soldered at the tip of a steel wire emerging through a ceramic insulating tube. Pulses 80–100 V in height and width 0.1 ms obtained by the circuit in Fig. 2(b) are applied at the exciter. It is possible[59] that solitons are excited by fluctuations of the grid sheath; however, since there is a large effective damping coefficient at pressures around 100 mTorr, the grid sheath fluctuations apparently serve only to perturb the plasma weakly in the region of our test section. At higher pressures (500 mTorr), the effect of the grid excitation seems to be more important.

(c) The *test section* consists of a hollow brass cylinder, to which are soldered three vacuum-quick couplers giving thereby the Langmuir probe geometry of Fig. 3. During a given run, the probes are biased in the ion saturation region and the fluctuating ion current is digitized and stored according to the schematic in Fig. 4. In addition, a conventional optical system is used to collect the light emission from the discharge near the test section. The object (point) in the test section is imaged on a 1-mm-diameter pinhole by a 5-cm focal length lens; the image is transferred by two 5-cm focal length lenses to a second 1-mm-diameter pinhole which contains a light pipe as the sensor in an EMI S-20 phototube. The light is used to check the disturbance created by the probe geometry, as discussed in Sec. III F.

(d) The *anode section* consists of a brass cylinder similar to the one described in Sec. III C above but sealed at one end. The grounded anode from the Voltronics power supply is attached to the anode section of the discharge.

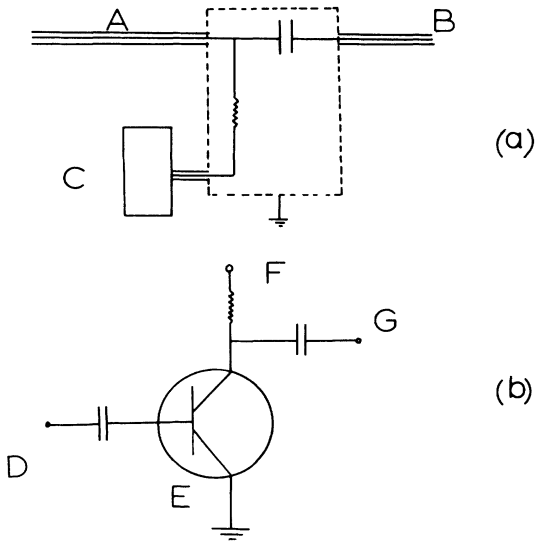

FIG. 2. (a) Probe circuit, shielded in a grounded aluminum box. $R=50$ kΩ and $C=0.25$ μF. A goes to the probe, B goes to the data acquisition system, and C is the probe bias which is a double polarity power supply. (b) High-voltage pulse generator. D is the pulse generator (width 0.1 ms, repetition rate 0.2–7.0 kHz) E is a transistor; F is a 80–100 V power supply, and G goes to the grid.

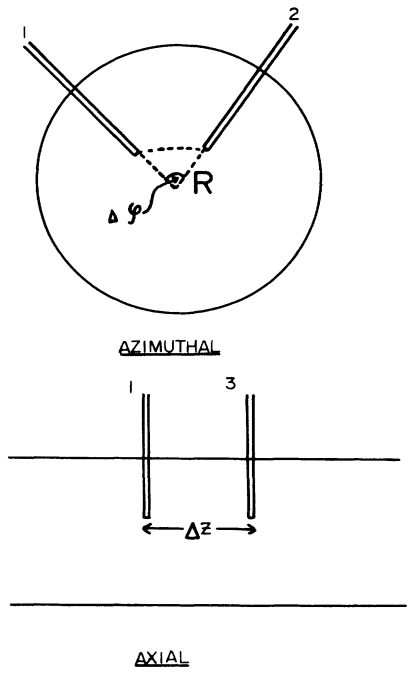

FIG. 3. Probe geometry showing azimuthal and axial configurations. $R\Delta\varphi=0.7854$ cm and $z=1$ cm. A fourth probe, diametrically opposite to probe 1 (P1) is inserted when measurements of ambipolar fields are to be made. Probes 1 and 3 are used to measure the axial field.

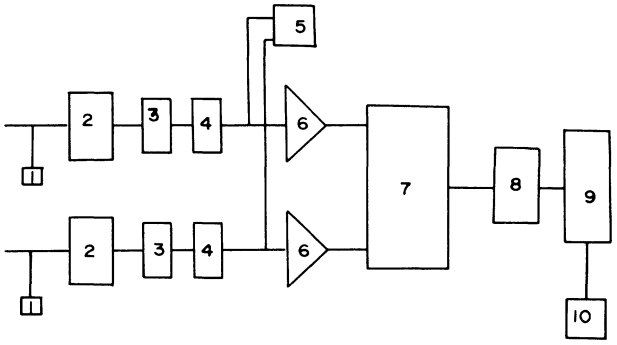

FIG. 4. Data acquisition system. 1 is a FLUKE digital multimeter, 2 is a probe circuit, 3 is a high pass filter, 4 is a low pass filter, 5 is an oscilloscope, 6 is a Biomation transient recorder, 8 is a Techtran floppy disc system, 9 is a DEC PDP-10, and 10 is an X-Y plotter.

The anode section is used in all probe diagnostics as a local reference for measurement of fluctuating plasma potential.

(e) The *extender sections* consist of Pyrex glass tubes which have the O-ring joint mentioned previously. There are five such pieces of length 10 cm and one piece of length 40 cm. These sections are placed between the cathode, exciter, and the test anode sections so as to provide intersection electrical insulation and to allow for some variation in the length of the positive column. Extreme care is exercised when joining the ends of these sections to other sections by ring clamps. A 3 mm layer of asbestos paper is wrapped around the neck of the joint before the ring clamp is applied.

B. Operating conditions

The various sections of the discharge tube are connected in sequence via the ring clamps and O rings on a bed of laboratory jacks—the latter being secured to a heavy optical table. The system is then pumped down to 10^{-5} Torr by an oil-diffusion pump. The initial pumpdown is maintained for a period of 30–36 hours, a time sufficient to allow the system to outgas completely. During this time the filament has been turned on. Then the system is filled with either argon, a mixture of argon and SF_6, or a mixture of argon and CO_2 to the desired pressure, and closed immediately after the filling. A discharge is initiated; when a gas mixture is used, a period of 5–10 min is allowed to elapse before the taking of any data. This period of time has seemed adequate so that the thermal diffusion and various ionic transport processes can produce uniformity in the mixtures.

C. Langmuir probes

Langmuir probes have been widely used as a diagnostic for plasma density fluctuations which are easily monitored when the probe is biased in the saturation regime.[7,8,10,49,52–57,60–62] Spatial and temporal behaviors can be obtained using two probe techniques.[57,60–62] From these results, cross-power and autopower spectra, correlations, dispersion relations, and nonlinear effects can be studied. In the present experiment, since we wish to study ion-density fluctuations in the positive column, we bias the probe to the ion-saturation voltage in order to collect ions[63–65] and produce the least disturbance to the ionized system. (Collecting electrons would provide a better frequency response but at the cost of too much current from the plasma.) We found typical values for the ion and electron currents to be and 300 mA in their respective saturation regimes.

Figure 2(a) gives a schematic description of the probe circuit. The probe bias voltage is supplied by a Gencom-Emitronics double polarity power supply. No ripple could be detected in the outputs of this power supply by our FLUKE-8000A digital multimeters (input impedance, 10 Ω). The whole circuit is shielded by aluminum boxes. BNC cables are used to convey the probe outputs from the test section to the bias unit and from these to the oscilloscope (Tektronics-545A) and the data acquisition system (Biomation 8100, Techtran 951). Noise at 60 Hz was reduced drastically by grounding the BNC and by using high-pass filters.

Sputtering on the probe tip seriously affects the probe's operation. As a part of the experimental procedure, probe characteristics were mapped over 40–50 runs. Part of the procedure involves biasing the probes strongly positive (orbital-limited region) to measure the density of negatively charged species. Under these accelerating conditions sputtering may occurre at the probes' tips. Under normal operation, i.e., in the ion-saturation regime, probe tips were inspected every week and the entire probe replaced in case of a major defect.

The probe is constructed with a 0.75-mm-diameter stainless steel wire, encased in a sheath of 1.5-mm outer diameter 99% Al_2O_3 ceramic insulator. One end of the probe is ground to a plane, flush with the sheath. The other end is soldered to a UG-1094/U BNC. The assembly is then inserted into a $\frac{1}{4}$ in. Teflon rod, which allows positioning of the probe tip in the discharge. The system is made vacuum tight by Torr-Seal and inserted into the quick coupler. This configuration has the advantage of a small local disturbance, high-frequency response, good spatial resolution, and a high-insulator work function; it suffers from very weak insulator mechanical strength and from handling difficulty.

From an operational point of view, Langmuir probes provide one of the simplest available methods for measuring local plasma properties. However, there are well-known inherent uncertainties in these probe measurements.[61,63–65] It was shown[61] by Powers that for 35 MeV $< T_e <$ 79 MeV, the electron temperature was systematically higher as compared to the more reliable spectroscopic measurements. This latter method cannot be used for local measurements of plasma properties. Chen and Schott have noted a 10% uncertainty in probe measurements. In summary, one is required to insure that the probe cause as little disturbance as possible to the discharge; the space occupied by its sheath and the current which it draws must be small compared to the volume and the current of the discharge.[14] Typical probe

currents for our experiment are 10 mA, compared to the discharge current of 100 mA. The ratio (r_p/L_D), where r_p is the probe radius and L_D is the Debye length, is approximately 50. A value of $(r_p/L_D) \gg 1$ assures that the probe causes the least possible disturbance to the plasma.

D. Data acquisition

The block diagram in Fig. 4 shows the arrangement of the data acquisition system. Two identical channels are available. Block 2 is the probe biasing circuit shown in Fig. 2(a). The FLUKE digital voltmeter, block 1 (input impedance 10 Ω), measures the probe bias with respect to the grounded anode in the plasma. Block 3 is a passive high-pass filter with cutoff at $f_0 = 120$ Hz, and is used to eliminate 60-cycle interference. Block 6 is a Hewlett Packard 465A wideband amplifier. The Biomation 8100 transient reorder (block 7) has a wideband analog-to-digital converter (ADC) and memory buffer which connects to the analog and digital parts of the data acquisition system. It has 50 and 5 MHz sampling frequencies for single- and chopped-mode operations. The input signal is digitized and stored in the memory. The memory has 2048 eight bit words to give 2048 sampling points in one run.

The well-known aliasing problem[50,51] is overcome by the passive low-pass filter (block 4) with cutoff at the Nyquist folding frequency. The digitized signal from the ADC was transferred to the floppy disc system (Techtran 951) shown in block 8, at 1200 baud. Each floppy disc is capable of holding 21 Biomation outputs, or runs. The collected data were transferred to a PDP-10 (block 9) via a modem at 300 baud. The data were then permanently stored on DEC tape and subsequently analyzed by our various computer programs.

E. Data analysis

The problem of analyzing fluctuation data associated with waves, instabilities, and turbulence may often be viewed in terms of identifying the various waves involved; i.e., one must measure the amplitude, frequency w, and wave vector k for each of the waves which may be simultaneously present in the plasma, and investigate the nonlinear interaction between them, if any. Previous studies dealing with analysis of plasma fluctuations have relied heavily on the use of the correlation function as indicated in the review by Hooper.[63] Generally speaking, such techniques are useful when only one wave is dominating the situation. Although, in principle, space-time correlation techniques may be utilized to measure w and $k(w)$, extensive analog filtering is required. In addition, prior knowledge of the fluctuation spectrum is required in order to set the passband of these filters. The feasibility of a digital implementation of a more general spectral analysis is due, in large part, to the advent of the fast Fourier transform[50-54] (FFT) and the economic feasibility of sophisticated data acquisition and processing hardware.

The time-sampled data can be transformed into the frequency domain via the discrete Fourier transform (DFT) defined by

$$G(f_k) = (1/N) \sum_{j=0}^{N-1} g(t_j) e^{-i2\pi jk/N} .$$

In the above, the quantity $g(t_j)$ is the real damped time-data function, and $G(f_k)$ is the corresponding DFT. The data consist of N sample points spaced at Δt sec apart. Consequently the sampling frequency is $f_s = 1/\Delta t$ Hz. The desired information lies in the frequency interval $0 < f < f_N$, where $f_N = f_s/2$ is the Nyquist frequency.

The FFT is an algorithm that enables one to carry out the DFT in a computationally efficient manner.[50-52] Detailed discussion of the FFT can be found in the literature.[51] The DFT (or FFT) possesses most of the properties of the CFT (continuous Fourier transform); however, some differences do arise as a result of the fact that sample waveforms of finite duration are being transformed. The Hanning window has been used extensively[49-52] to solve this problem and is easily implemented in our analyses. In summary, the Hanning window imposes very low side lobe levels onto the $[\sin(x)/x]$ form which substantially reduce the leakage problem. Furthermore, it can be easily implemented in terms of a simple weighted average in the frequency domain.

In the situation of interest to us, we have two probes situated at r_1 and r_2 in the plasma. The probe signals can be represented by

$$\begin{aligned} g_1(\mathbf{r}_1,t) &= \sum_w g_1(w)\exp\{i[\mathbf{k}(w)\cdot\mathbf{r}_1 - wt]\} , \\ g_2(\mathbf{r}_2,t) &= \sum_w g_2(w)\exp\{i[\mathbf{k}(w)\cdot\mathbf{r}_2 - wt]\} . \end{aligned} \tag{1}$$

Writing

$$G_1(w) = g_1(w)\exp\{i[\mathbf{k}(w)\cdot\mathbf{r}_1]\} , \tag{2}$$

Eq. (1) can then be written as

$$g_1(\mathbf{r}_1,t) = \sum_w G_1(w)\exp(-iwt) .$$

Similarly,

$$g_2(\mathbf{r}_2,t) = \sum_w G_2(w)\exp(-iwt) .$$

G_1 and G_2 are in general complex. Then the *autopower* spectrum is given by

$$\begin{aligned} P_{11} &= G_1^*(w)G_1(w) = |G_1(w)|^2 , \\ P_{22} &= G_2^*(w)G_2(w) = |G_2(w)|^2 . \end{aligned}$$

The associated *cross-power* spectrum is

$$\begin{aligned} P_{12} &= G_1^*(w)G_2(w) = \alpha + i\beta \\ &= |P_{12}|\exp(i\theta_{12}) , \end{aligned}$$

where

$$|P_{12}| = (\alpha^2+\beta^2)^{1/2}, \quad \theta_{12} = \tan^{-1}(\beta/\alpha) .$$

Referring to Eq. (1). we note that

$$G_1^*(w)G_2(w) = |P_{12}|\exp[i\mathbf{k}(w)\cdot\Delta\mathbf{r}] .$$

Comparing with Eq. (2), we identify

$$\mathbf{k}(w)\cdot\Delta\mathbf{r}=\theta_{12}$$

or

$$k_i(w)=\theta_{12}/\Delta r_i \ . \tag{3}$$

Thus Eq. (3) allows the determination of the wave vector $\mathbf{k}(w)$ along a chosen unit vector i to be determined from the phase difference between the two probe signals. As mentioned in Sec. III A above and indicated in Fig. 3 the probes are placed in the axial and azimuthal geometry. Equation (3) allows the determination of the axial and azimuthal wave vectors of the plasma waves, i.e.,

$$k_z(w)=\theta_{12}/\Delta z, \quad k_\sigma(w)=\theta_{12}/R\,\Delta\varphi \ .$$

The associated axial and azimuthal phase velocities are

$$v_z^{\rm ph}=w/k_z, \quad v_\sigma^{\rm ph}=w/k_\sigma \ .$$

The group velocities may be obtained from the slope of Eq. (3)

$$v_z^{\rm gr}=dw/dk_z, \quad v_\sigma^{\rm gr}=dw/dk_\sigma \ .$$

Knowledge of the phase and group velocity helps in identifying the wave. Furthermore, the ability to experimentally determine w and k for each of the several waves simultaneously present in the plasma is useful for the study of wave-wave interaction.

Several theories and experiments concerned with the spectrum of plasma turbulence indicate that in the turbulent state, the power spectra falls off as k^{-n}. Roth[66] and others[67] have noted a large spread in the values of n, $1<n<7$. It is possible to determine experimentally the spectral index n from the power spectra, and determine if the plasma in our discharge is turbulent.

Other information can be routinely extracted from the FFT's. The auto- and cross-correlation functions $C_{11}(\tau)$, $C_{22}(\tau)$, and $C_{12}(\tau)$ can be determined by taking the inverse Fourier transform of the corresponding power spectra,

$$C_{12}(\tau)=\int g_1(t)g_2(t+\tau)dt \ .$$

From this process various correlation times may be obtained. Furthermore, the information on the growing and damping of each mode in the spectrum is buried in the sideband of the mode. Digital bandpass filtering can be be easily applied to get the history of a specified mode. We apply a FFT first then an inverse FFT only on the band in which we are interested. This filtering is accomplished in the Fourier space instead of real space. After the filtering the evolution of each mode can be observed

The spectral techniques indicated above are of limited value when various spectral components interact with one another due to some nonlinear process. However, one such nonlinear process, the wave-wave interaction,[53,54] is particularly well suited for detection by a digital bispectral analysis. Specifically, in a power spectra analysis, it is not possible to determine if the various modes present in the spectrum are independently generated modes or if they arise due to mode-mode coupling. If a wave-wave interaction exists between a set of modes in the system, then there is a definite phase coherence between these modes. The detection of such phase coherence is carried out by the bispectral analysis.

The wave-wave interaction selection rules[11,12,19] are

$$w_1\pm w_2=w_3 \ ,$$

$$\mathbf{k}_1\pm\mathbf{k}_2=\mathbf{k}_3 \ .$$

Defining the bispectrum as

$$B(w_1,w_2)=E(X(w_1)X(w_2)X^*(w_1+w_2)) \ ,$$

where E is an expectation value operator and $X(w_i)$ is the Fourier transform of mode w_i (obtained by the FFT), we can see that the bispectrum measures the statistical dependence between the three waves. If w_1,w_2,w_1+w_2 are three independent modes of the system, each mode would be characterized by a statistically independent random phase. Hence the sum of the phases

$$\sigma_1+\sigma_2=\sigma_{1+2}$$

would be randomly distributed over $(-\pi,\pi)$. When the averaging denoted by E is carried out, the bispectrum would vanish. On the other hand, if the components are nonlinearly coupled to each other, the phases of the three waves will not be random at all, and averaging will yield a nonzero value of the bispectrum. A quantitative measure of the phase coherence may be obtained by defining the bispectrum as[53]

$$b^2(w_1,w_2)=\frac{|B(w_1,w_2)|^2}{P(w_1)P(w_2)P(w_1+w_2)} \ .$$

Thus $b^2\to 1$ if wave-wave interaction exists; $b^2\to 0$ otherwise.

The coupling coefficient for these interactions may be defined by

$$X_{w3}=\mathcal{C}(1,2)X_{w1}X_{w2} \ ,$$

where w_1,w_2,w_3 satisfy the selection rules. Multiplying each side of the equation by $X_{w1}^*X_{w2}^*$ and taking an expectation value, we get

$$\mathcal{C}(1,2)=\frac{B^*(w_1,w_2)}{E(|X_{w1}X_{w2}|^2)} \ .$$

In the digital implementation of the power spectra, correlation function and the bispectrum are computed in these procedures, computed along with the autopower cross-power and the phase (dispersion) spectra. The input data (2048 points per run, 1 MHz sampling rate), corresponding to the probe fluctuations in the two geometries described, are normalized as follows: the height of the largest peak in the input is determined and then the rest of the data is divided by this number. This is done for each channel and for all the runs. Data smoothing is done by adjacent smoothing[52] in frequency domain. The spectral indices n are obtained by taking the log of the cross-power spectrum, and by subsequently determining the slope of this curve for values of 200 kHz $<f<$ 400 kHz, by a least-squares method. The input data is split into 32 sets, each consisting of 64 points each. A Hanning window (as discussed above) is applied to each data

set to reduce leakage. The bispectrum is then computed for each set by the equation described in this section and then an average of the 32 sets is taken.[53,54] The cross-correlation function is obtained and normalization is performed on the input in the time domain, as described earlier.

F. Calibration

In Fig. 5(a) is plotted the voltage drop V_p as I_d changes by a factor of 2, confirming, that in this region a normal glow discharge exists. Figure 5(b) shows plots of the total discharge voltage V_d versus the gas pressure for the cases when pure Ar and when a mixture of Ar and SF_6 (10% concentration) are present in the discharge. As indicated, there is a significant change in V_d at higher pressures. The electron drift velocity decreases as the pressure increases.[14,22] As the discharge is maintained by a constant current source, V_d increases with pressure, thereby increasing the electron drift velocity and thus maintaining the same current.

The electron temperature T_e is measured by biasing the probe negatively with respect to the plasma.[63,65] T_e so obtained is shown in Fig. 5(d), plotted against the discharge pressure. The curve allows the Schottky profile,[1,14,22] thus verifying that in the region of pressures that are of interest, diffusion is a prominent charged-particle transport process. The electron concentration is measured by biasing the probe positive into the orbital-limited region.[68–72]

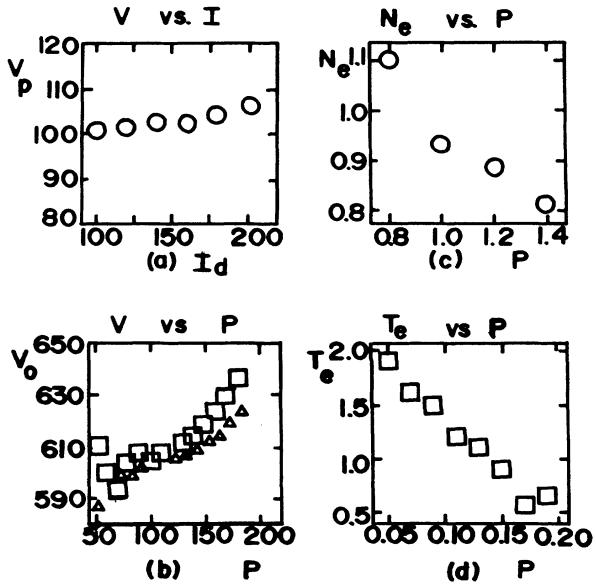

FIG. 5. (a) Voltage drop (V_p volts) across the positive column vs discharge current I_d (mA). (b) Voltage drop (V_0 volts) across the discharge tube vs the gas pressure in the tube (mTorr). The large square is Ar only; the small symbol is a 10% SF_6 mixture of (AR + SF_6). (c) Electron concentration (in units of 10^{10} cm^{-3}) vs gas pressure (in units of 10^{-1} Torr). (d) Electron temperature (eV) vs gas pressure (Torr).

The probe characteristics so obtained are shown in Fig. 6(a) where electron current i_e^2 is plotted against the probe potential. Shown are the plots obtained for various pressures of Ar gas. The slope in the linear region gives[68–72] the electron concentration N_e. Thus a plot of N_e versus the gas pressure is obtained, as shown in Fig. 5(c).

Biasing the probe in the orbital-limited region allows a determination of negative-ion concentration.[68–72] Shown in Fig. 6(b) are the i_e^2 versus pressure plots for gas mixtures with various concentrations of SF_6. The slopes in the linear region give[70] the modified electron concentration N_e'. Hence, an estimate of the negative-ion concentration N_{SF6} is obtained by $N_e - N_e'$. In this way, a plot of N_{SF6} versus gas pressure is obtained. Figure 6(c) shows such a plot for three different mixtures.

These results seem to show that the electron concentration goes down as the gas pressure is increased, and the negative-ion concentration increases with pressure. Two further independent tests are made to support this result. For this, we recall that diffusion theory predicts[22] an ambipolar field in the radial direction of magnitude

$$E_r = (kT_e/e)(1/n)(dn/dr) ,$$

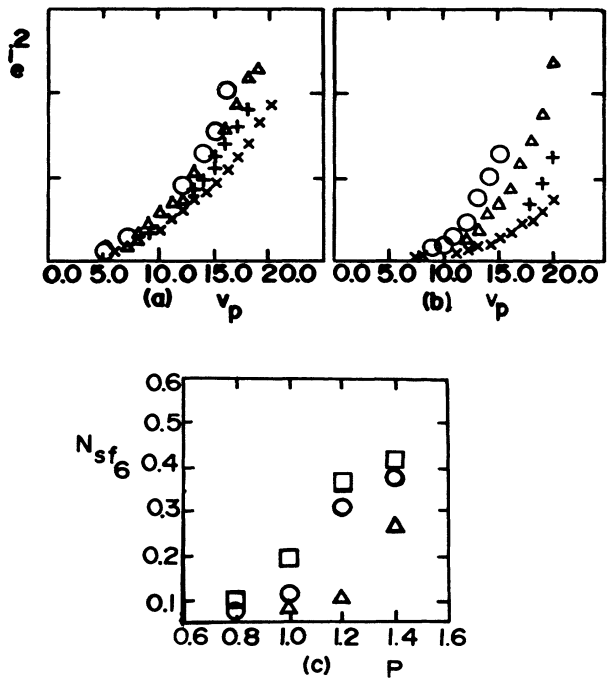

FIG. 6. (a) Plot of i_e^2 and probe bias V_p (volts) for various discharge gas pressures. × represents 140 mTorr; the others are ○, 120 mTorr; △, 100 mTorr; and +, 80 mTorr. (b) Plot of i_e^2 and probe bias V_p (volts) for various discharge mixture pressures (with 15% SF_6). Total pressures are the same as in (a) above, i.e., × represents 140 mTorr, etc. (c) Plot of negative-ion concentration $N(SF_6)$ (units of 10^{10} cm^{-3}) and gas pressures for various mixtures. □ (topmost) 20% SF_6; ○ (inner) 15% SF_6; △ (bottom) 5% SF_6.

where

$$n(r)=n_0 J_0(2.405r/R)\ ,$$

R being the radius of the discharge. In the presence of negative ions, of concentration N_n, the ambipolar field is modified and given by[18,21]

$$\frac{E_r(\alpha)}{E(\varphi)}=\frac{1-(D^+/D_a)}{1+\alpha}\left[\frac{1+\gamma}{\gamma}\right],$$

where $\alpha=N_n/N_e$, $\gamma=T_e/T^+$, and D^+,D_a are the ionic and ambipolar diffusion coefficient. Assuming r remains constant, this equation implies that the ambipolar field decreases as N_n increases.[18,21]

The ambipolar field ratio (above) was determined in our experiments and is plotted as a function of gas pressure, Fig. 7(b), for various mixtures. By this plot it can be concluded that the ratio and p are directly related.

The plasma current density j and axial electric field E_z are related by[73]

$$E_z=m_e\nu_c j/n_e e^2\ .$$

Since the discharge is maintained by constant current supply, j is constant. (This has been verified experimentally to 1 mA, the discharge current being 100 mA. The discharge radius is constant; hence, the discharge current and current density are equivalent.) The above equation implies that if N_e should decrease, E_z must increase to maintain constant j. Such a decrease could arise from attachment or decrease in electron temperature. If the latter effect were to be accounted for in a measurement of E_z, any anomalous variation in E_z would imply another loss process for the discharge electrons.

The axial electric field was measured versus the gas pressure for various mixtures and for the case when no SF_6 was present in the discharge. The results are displayed in Fig. 7(a). Shown also are the plots for three mixtures of varying SF_6 concentration. The lowest trace (X) shows the variation of E_z with pressure for Ar only. An increase in E_z with increasing p in this case results from a decrease in the ionization rate. Addition of SF_6 results in a further increase in E_z at a given pressure.

The results presented in Figs. 6 and 7 and the corresponding discussion allow us to conclude that some process other than ionization loss is present. This process appears to have a greater influence as p is increased. The only important loss process for the discharge electrons under these conditions is attachment. We again note that increasing p is the same as increasing the negative-ion concentration.

Finally, as mentioned in Sec. III A, a check is made to confirm that the probes reflect the fluctuations in the plasma. Because of the Debye sheath formed around the

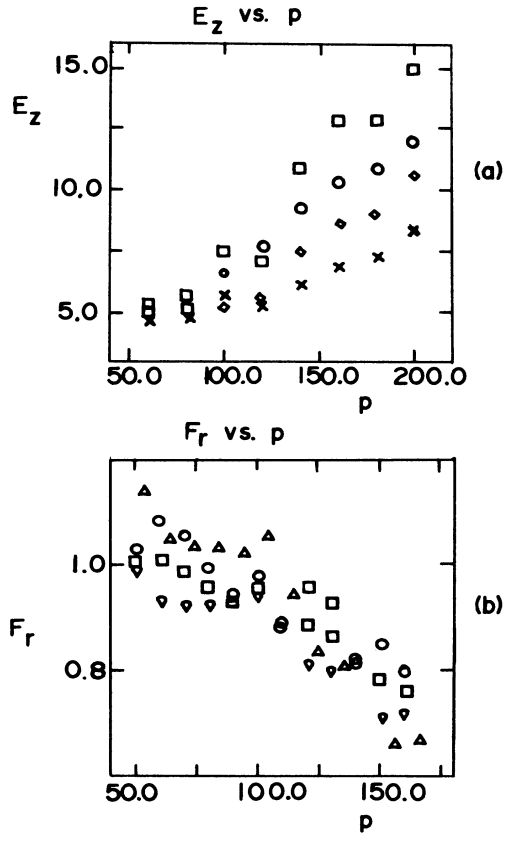

FIG. 7. (a) Axial electric field and gas pressure for various mixtures of SF_6. The topmost □ is 20% SF_6; the successive symbols are ○, 15% SF_6; ◇, 10% SF_6; and ×, 0% SF_6, respectively. (b) ratio of ambipolar field in the presence of negative ions of SF_6 to ambipolar field in argon only $[F_r=E_r(\text{Mix})/E_r(0)]$ and gas pressure for various mixtures. □ is a 10% mixture of SF_6; ○ is 5%; ◇ (bottom) is 20%; △ (topmost) is 15%.

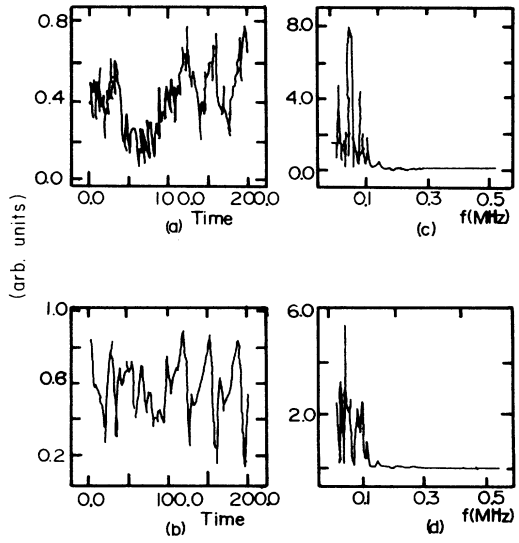

FIG. 8. (a) Ion density fluctuations collected by a probe biased in the ion-saturation regime vs time (μ sec). (b) Light fluctuations from the photomultiplier and time (μ sec). (c) Power spectrum of (a) above. (d) Power spectrum of (b) above.

probe surface, it is to be expected that probe potential would be significant only for a few Debye lengths.[63] Hence, the probe would act like a true "probe," i.e., it has negligible effect on the system (in the present case, by picking up the fluctuating ion current that passes through the Debye sphere).

A conventional optical system is used to probe the plasma. As the light collection causes no disturbance to the system, these data were compared against the probe output. The simultaneous outputs of the photomultiplier tube (PMT) and a probe (biased in ion-saturation regime) are collected and analyzed. Figures 8(a) and 8(b) show the digitized outout of the probe and PMT, respectively. Since the probe is a point diagnostic and the light output shows averaging, consequently it appears smoother. Similar results were obtained by Dieke.[5] The corresponding autopower spectra are shown in Figs. 8(c) and 8(d). Notice that rough peak-to-peak correspondence is present in the raw output and the autopower spectra signatures agree. These results confirm that the probe is a valid point diagnostic.

IV. RESULTS

A. Ion-current profiles and two probe measurements

Typical normalized probe currents are displayed in Fig. 9. Shown are the first 500 μsec of the digitized data in

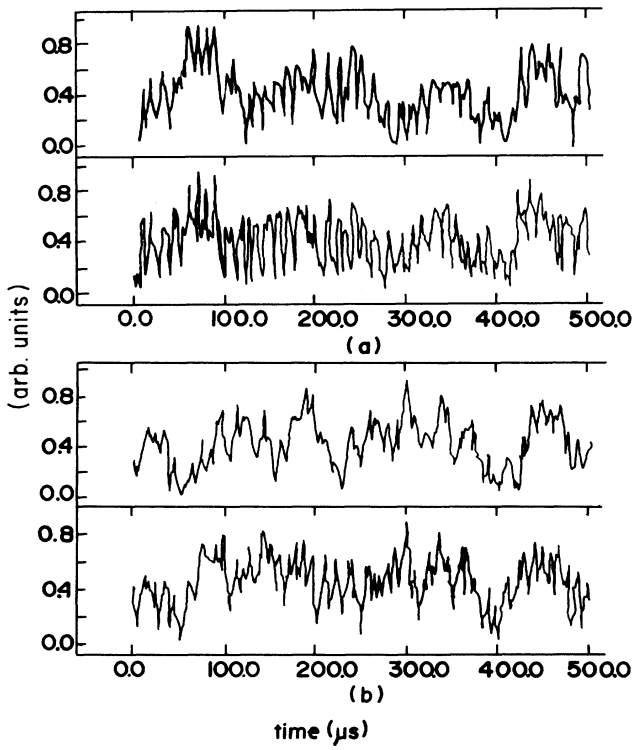

FIG. 9. Samples of saturated ion current vs time. These are taken with the axial geometry; the upper trace is from probe P3 and the lower trace is from probe P1. (a) Gas pressure is 80 mTorr and 20% SF_6. (b) Gas pressure is 160 mTorr and 20% SF_6.

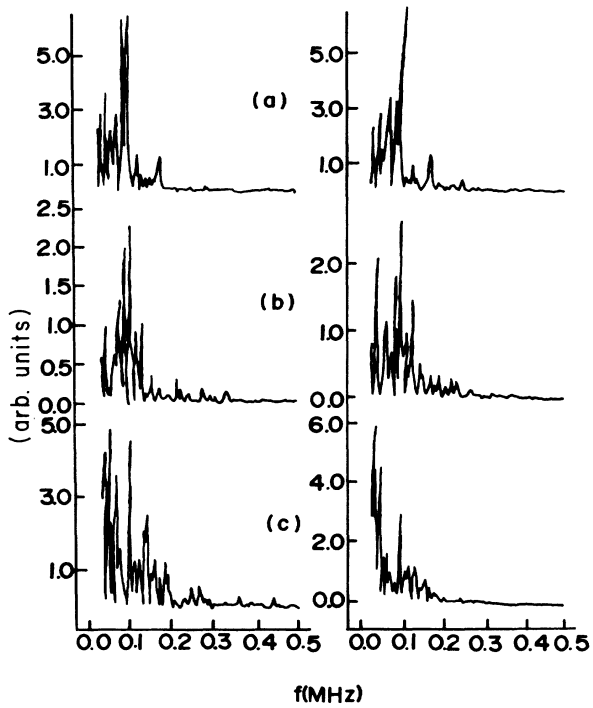

FIG. 10. Samples of autopower spectra for the azimuthal geometry. Left trace is the spectrum of probe P1 (P_{11}). Right trace is the spectrum of probe P2 (P_{22}). (a) Gas pressure = 80 mTorr with 5% SF_6. (b) Gas pressure = 120 mTorr with 5% SF_6. (c) Gas pressure = 160 mTorr with 5% SF_6.

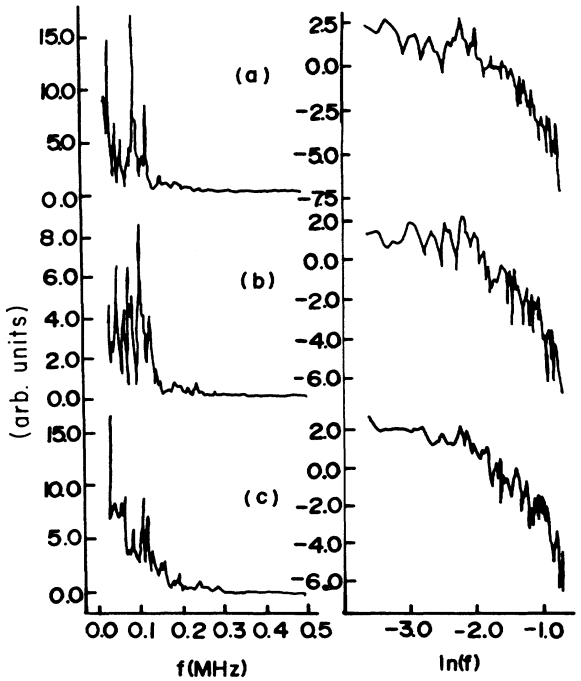

FIG. 11. Samples of cross-power spectra for the azimuthal geometry. Left trace is the cross-power spectrum (P_{12}). Right trace is $\ln(P_{12})$ vs $\ln(f)$. (a), (b), and (c) are (as in Fig. 10) for 80, 120, and 160 mTorr gas pressure and 5% SF_6.

each channel of the ADC (full length 1024 μsec). The probes are in the axial geometry for each figure, the gas being a mixture of Ar and SF_6. As suggested in the figure, the higher-pressure runs had more complex waveforms than corresponding low-pressure runs. Furthermore, a higher number of large structures may be seen in the high-pressure runs. This is typical behavior in these data, reminiscent of large coherent structures often seen in turbulent flow.[74–76]

1. Concerning SF_6

Figures 10–12 are the results of the autopower, cross-power, and phase-spectral analysis when the gas mixture in the discharge is Ar with varying concentration of SF_6. The probes are in the azimuthal geometry as shown in Fig. 3. It is evident from our autospectra that, as the gas-mixture pressure is increased for a given concentration of SF_6, the number of high-frequency components increases and then (near 160 mTorr) decreases. Furthermore, the amplitudes of some of the modes decrease as the waves travel in the azimuthal plane from P1 to P2. This shows that the azimuthal damping, which is not very strong at low pressures, increases with pressure until a regime is reached in which only the long-wavelength components tend to survive. In addition, as the concentration

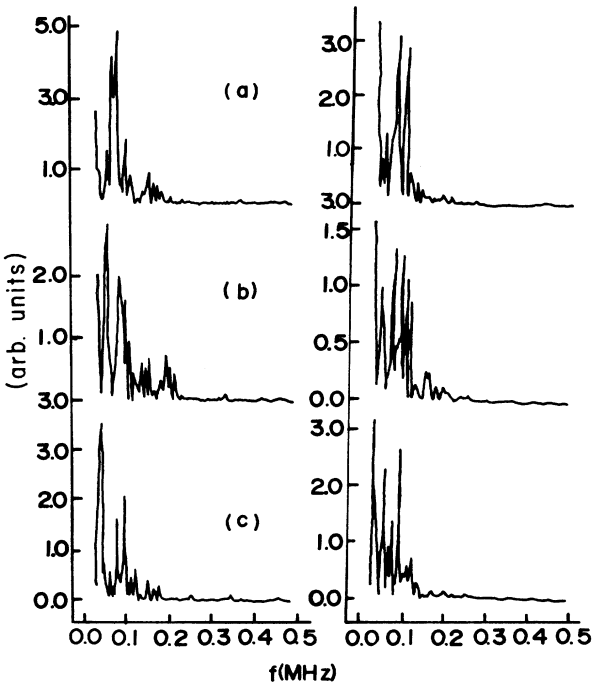

FIG. 13. Samples of autopower spectra for the axial geometry. Left trace is the spectrum of probe P1 (P_{11}). Right trace is the spectrum of probe P3 (P_{33}). (a), (b), and (c) are for gas pressures 80, 120, and 160 mTorr, respectively, and 5% SF_6.

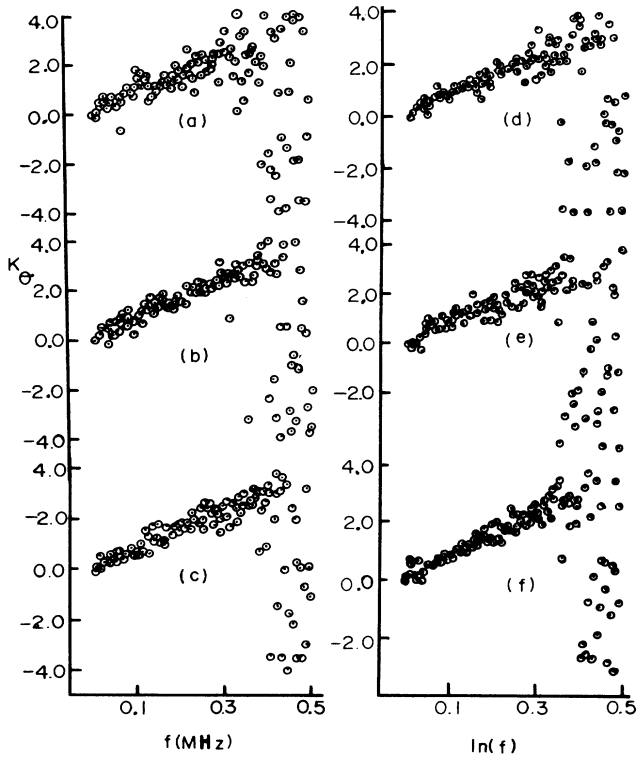

FIG. 12. Samples of dispersion relations for the azimuthal geometry: k_θ (cm^{-1}) vs frequency (MHz). (a) and (d) are at 80 mTorr gas pressure, (b) and (e) are for 120 mTorr gas pressure, and (c) and (f) are for 160 mTorr gas pressure. (a), (b), and (c) have 5% SF_6; (d), (e), and (f) have 20% SF_6.

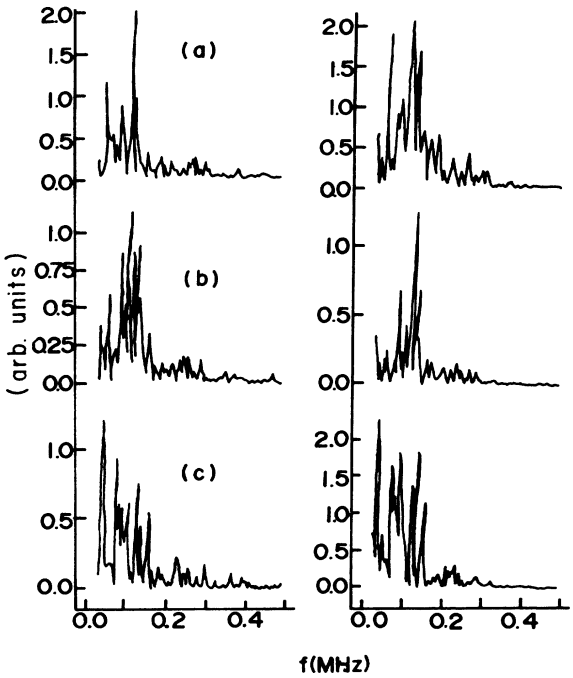

FIG. 14. Samples of autopower spectra for the axial geometry. Left trace is the spectrum of probe P1 (P_{11}). Right trace is the spectrum of probe P3 (P_{33}). (a), (b), and (c) are for gas pressures 80, 120, and 160 mTorr, respectively, and 20% SF_6.

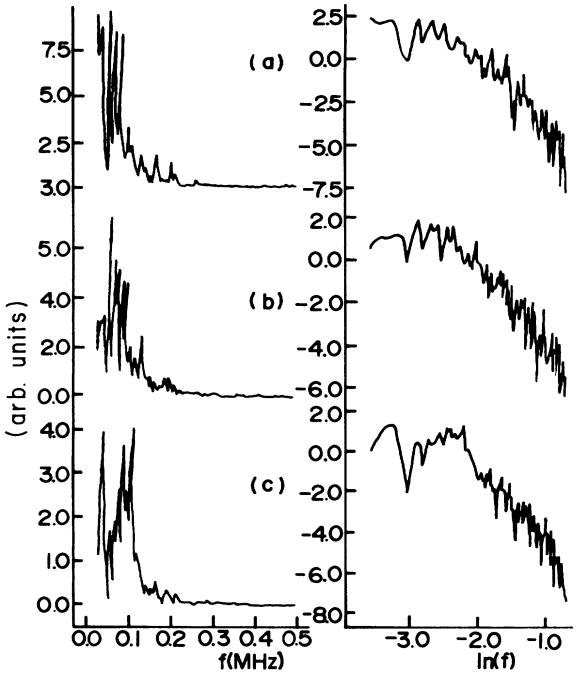

FIG. 15. Samples of cross-power spectra for the axial geometry. Left trace is the cross-power spectrum (P_{13}). Right trace is $\ln(P_{13})$ vs $\ln(f)$. (a), (b), and (c) are (as in Fig. 13) for 80, 120, and 160 mTorr gas pressure and 5% SF_6.

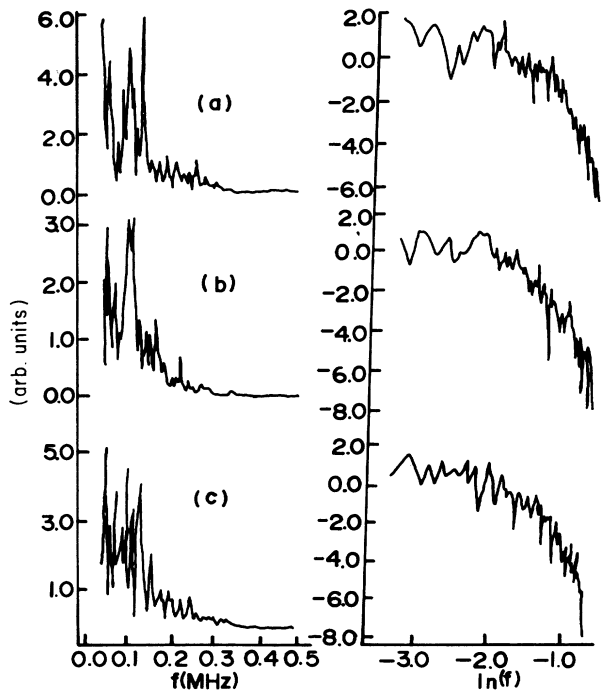

FIG. 16. Samples of cross-power spectra for the axial geometry. Left trace is the cross-power spectrum (P_{13}). Right trace is $\ln(P_{13})$ vs $\ln(f)$. (a), (b), and (c) are (as in Fig. 14) for 80, 120, and 160 mTorr gas pressure and 20% SF_6.

of SF_6 is increased from 5% to 20%, the number of high-frequency modes increased for a given pressure.

The cross-power spectra also show the same trends. The number of modes that are common to both P1 and P2 first increases with pressure, as above, and then decreases. The number of high-frequency modes increases with an increase in SF_6 concentration for a given mixture pressure. The logarithmic plots, $\ln(P_{12})$ versus $\ln(f)$, are used to estimate the spectral index[67] which will be discussed later.

The dispersion relation plots show that k_θ is roughly linearly proportional to w, especially in the low-frequency regions. However, for those mixture pressures and concentrations for which the autopower and cross-power spectra exhibit enhanced production of high-frequency components, the dispersion relation deviates remarkably form linearity. Nonetheless, the quasilinear behavior is always regained as the pressure is increased.

The set of Figs. 13–17 gives examples of the results of the autopower, cross-power, and phase spectral analysis when the probes are in the axial geometry. The same qualitative features are observed as in Sec. IV A. However, there is relatively little attenuation in the axial direction for all pressures as compared to the azimuthal case. The damping coefficient in the axial direction appears to

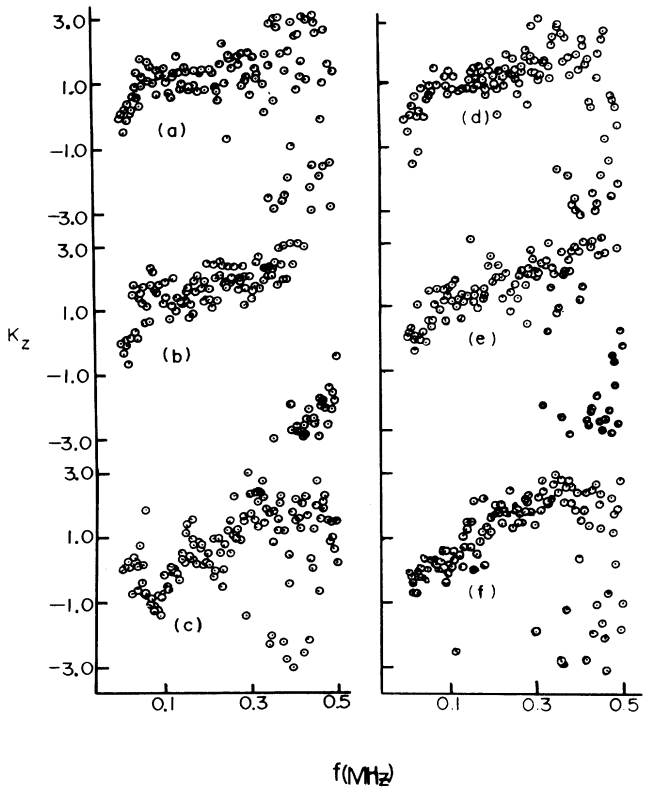

FIG. 17. Samples of dispersion relations for the axial geometry k_z (cm^{-1}) vs frequency (MHz). (a) and (d) are at 80 mTorr gas pressure, (b) and (e) are for 120 mTorr gas pressure, and (c) and (f) are for 160 mTorr gas pressure. (a), (b), and (c) have 5% SF_6; (d), (e), and (f) have 20% SF_6.

be less sensitive to variation in pressure. The cross-power spectra and the autopower spectra show a different high-pressure behavior. For a given concentration of SF_6, as the pressure increased, the number of high-frequency modes increase (up to 160 mTorr, as shown). For a given pressure, as the gap additive concentration (SF_6) is increased, the number of modes also increases even at high pressures. The dispersion relations exhibit a deviation from linearity at increasing pressures for a given concentration of SF_6. Only the low-pressure cases suggest linearity.

2. *Concerning CO_2*

Figures 18–22 are samples of the results of the autopower, cross-power, and phase spectral analysis. The gas mixture in the discharge is Ar with varying concentrations of CO_2. The probes are in the axial geometry as defined in Fig. 3. The results here are different from those for SF_6. In the CO_2 autopower spectra, only the low-pressure (40 mTorr) traces exhibit enhanced mode generation at high frequencies. There is a systematic decrease in the number of modes at high frequencies as the pressure is increased for a given concentration. For a given pressure, the number of modes increases with an increase in the amount of CO_2 in the system. The cross-power spectrum exhibits the same features. The dispersion relations show that the system is definitely nonlinear at low pressures and that it exhibits quasilinearity at high pressures.

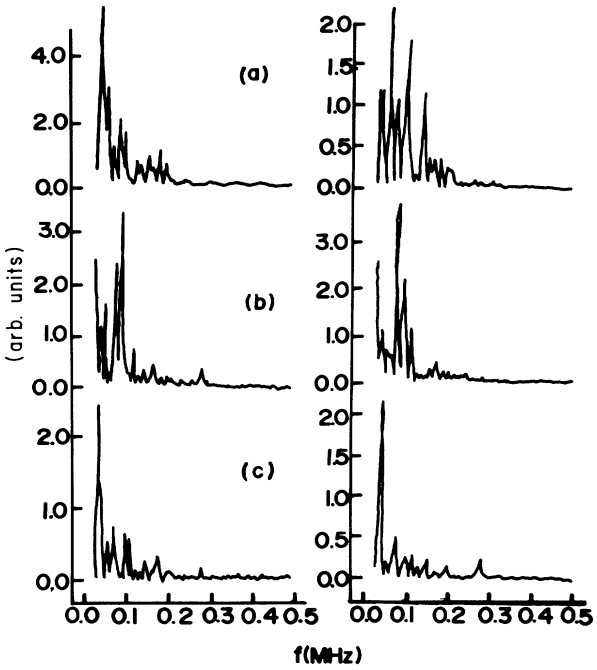

FIG. 19. Samples of autopower spectra for the axial geometry. Left trace is the spectrum of probe P1 (P_{11}). Right trace is the spectrum of probe P3 (P_{33}). (a), (b), and (c) are for gas pressures 60, 100, and 160 mTorr, respectively, and 20% CO_2.

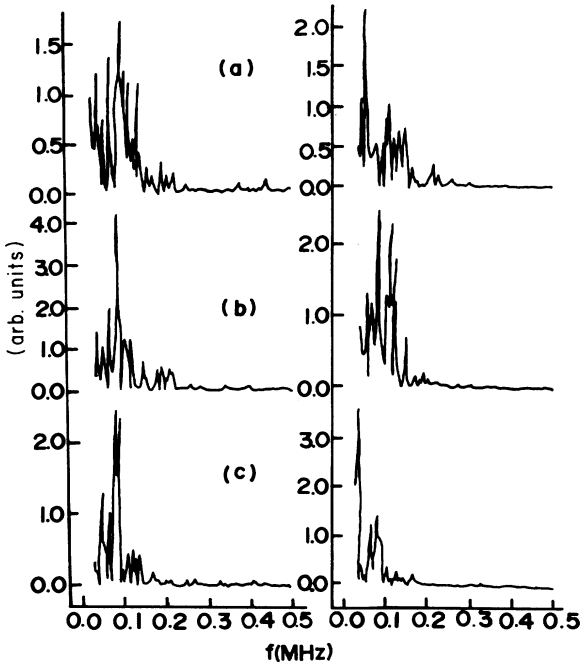

FIG. 18. Samples of autopower spectra for the axial geometry. Left trace is the spectrum of probe P1 (P_{11}). Right trace is the spectrum of probe P3 (P_{33}). (a), (b), and (c) are for gas pressures 60, 100, and 160 mTorr, respectively, and 5% CO_2.

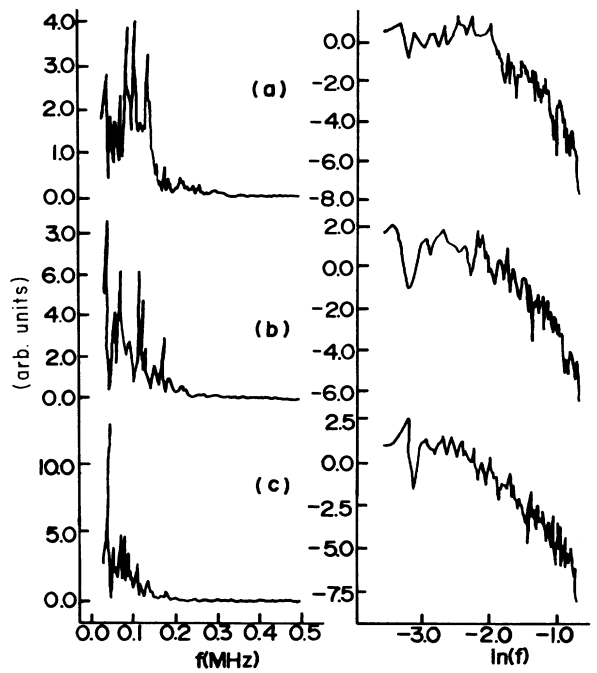

FIG. 20. Samples of cross-power spectra for the axial geometry. Left trace is the cross-power spectrum (P13). Right trace is ln(P13) vs ln(f). (a), (b), and (c) are for 60, 100, and 160 mTorr gas pressure and 5% CO_2.

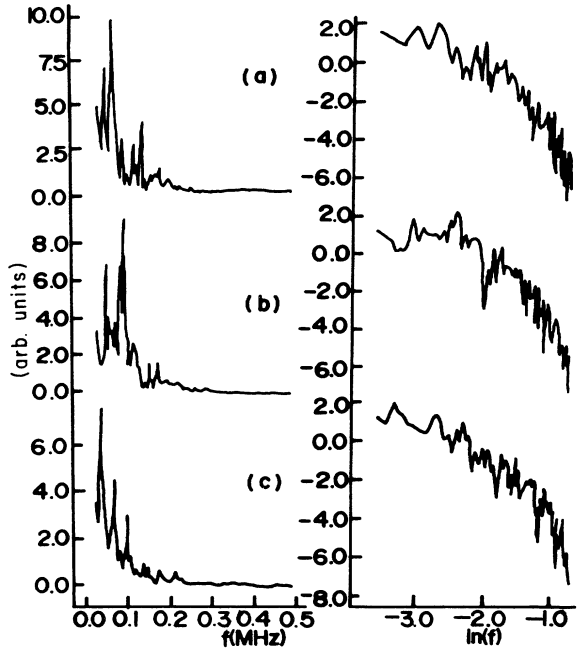

FIG. 21. Samples of cross-power spectra for the axial geometry. Left trace is the cross-power spectrum (P13). Right trace is ln(P13) vs ln(f). (a), (b), and (c) are for 60, 100, and 160 mTorr gas pressure and 20% CO_2.

When the probes are in their azimuthal geometry and the gas in the discharge is Ar with varying concentrations of CO_2, the same general features of the data from the preceding paragraphs are repeated. Specifically, the same kind of striking change in the autopower spectrum is shown. The cross-power spectra also exhibit the trend. Furthermore, the dispersion relations imply strong nonlinearity for the low-pressure case and increasing linearity for high pressures.

B. Cross-correlation spectral and bispectral analysis

Figures 23 and 24 give examples of the cross-correlation function versus time (μsec) for the axial probe geometries. The runs in this study have varying amounts of SF_6. Figure 24 represents one of the cases when CO_2 is the additive. For a given concentration of SF_6, we see that at low pressures the dominant mode is present in large amounts for the entire data sampling time (1024 μsec). As the pressure is increased, the magnitude of the correlation coefficient goes down, and higher harmonics of the dominant mode appear as time increases. For a given concentration of CO_2, it seems that the dominant mode is decomposed into higher harmonics at low pressures (40 mTorr) and as the pressure increases, the mode is sustained for a longer time.

Figures 25 and 26 are plots of the spectral index n versus pressure for various concentrations of SF_6 and CO_2

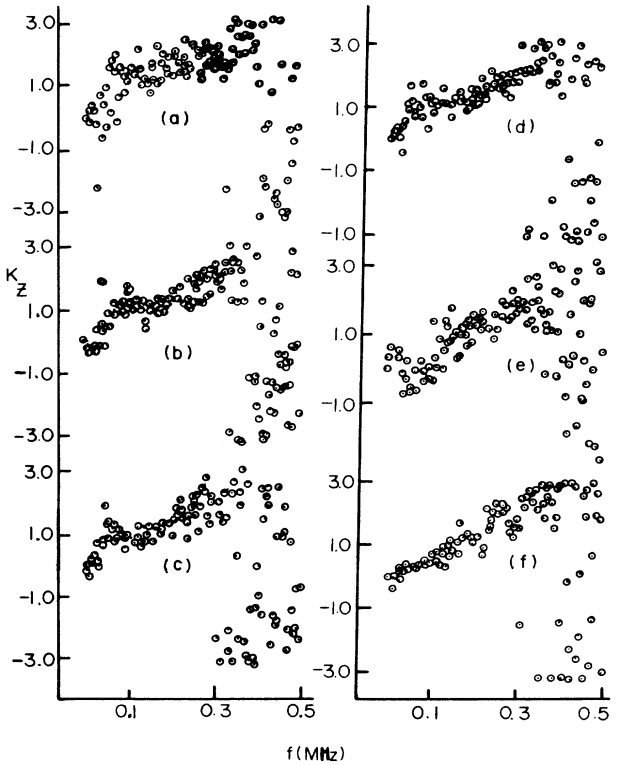

FIG. 22. Samples of dispersion relations for the axial geometry K_z (cm^{-1}) vs frequency (MHz). (a) and (d) are at 60 mTorr gas pressure, (b) and (e) are for 100 mTorr gas pressure, and (c) and (f) are for 160 mTorr gas pressure. (a), (b), and (c) have 5% CO_2; (d), (e), and (f) have 20% CO_2.

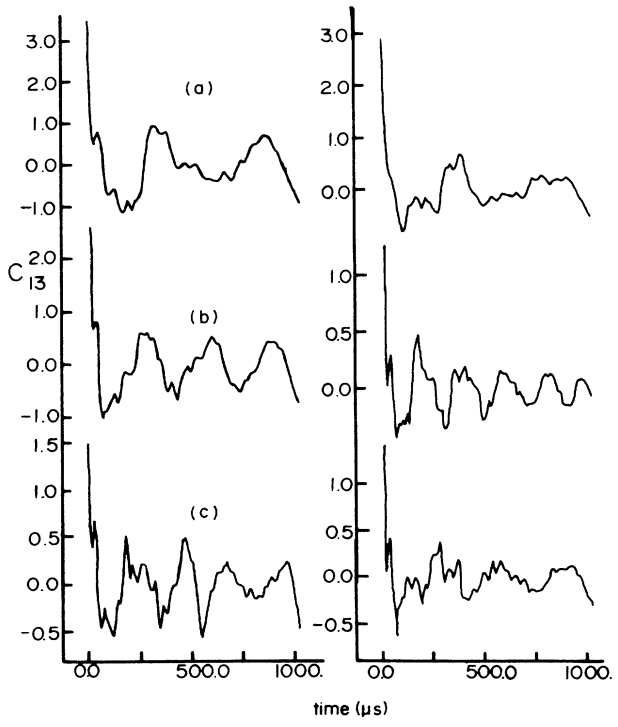

FIG. 23. Cross-correlation function C_{13} vs time. (a) 50 mTorr gas pressure: left trace is 5% SF_6, right trace is 20% SF_6. (b) 100 mTorr gas pressure: left trace is 5% SF_6, right trace is 20% SF_6. (c) 160 mTorr gas pressure: left trace is 5% SF_6, right trace is 20% SF_6.

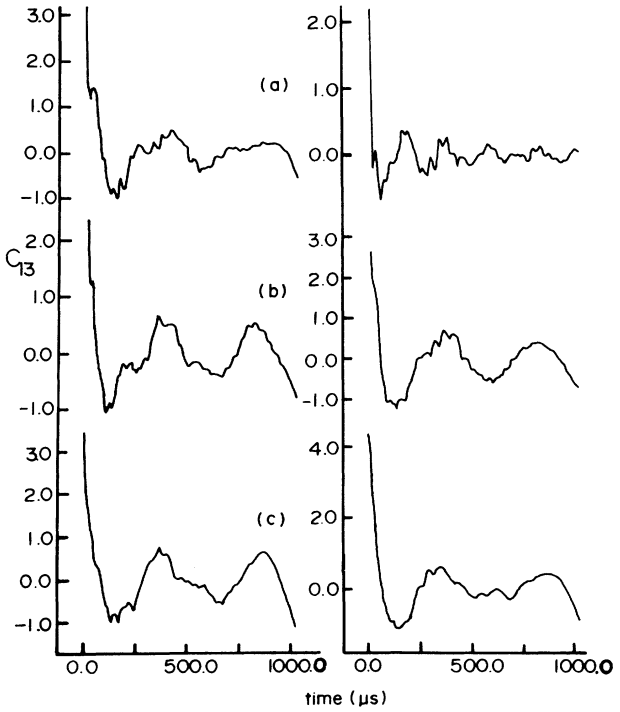

FIG. 24. Cross-correlation function C_{13} vs time. (a) 60 mTorr gas pressure: left trace is 5% CO_2, right trace is 20% CO_2. (b) 100 mTorr gas pressure: left trace is 5% CO_2, right trace is 20% CO_2. (c) 160 mTorr gas pressure: left trace is 5% CO_2 right trace is 20% CO_2.

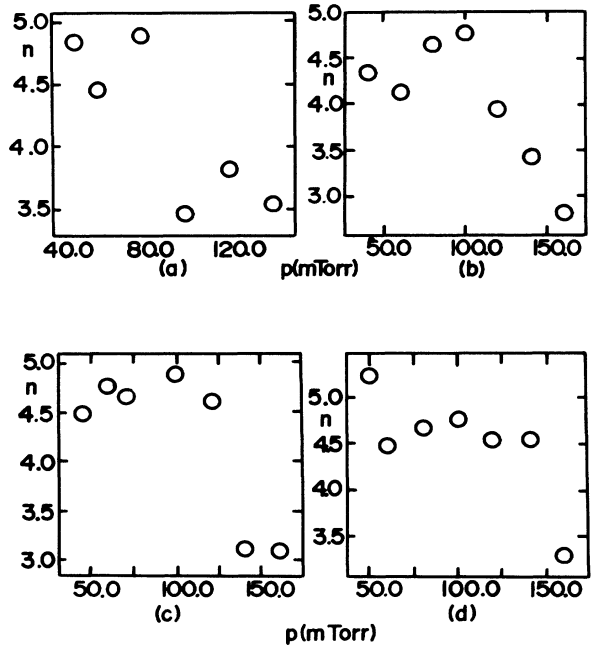

FIG. 25. Spectral indexes: axial geometry. Plots are given of spectral index n vs pressure (mTorr) for frequencies between 200 and 400 kHz. (a), (b), (c), and (d) are for mixtures of 20%, 16%, 10%, and 5% SF_6.

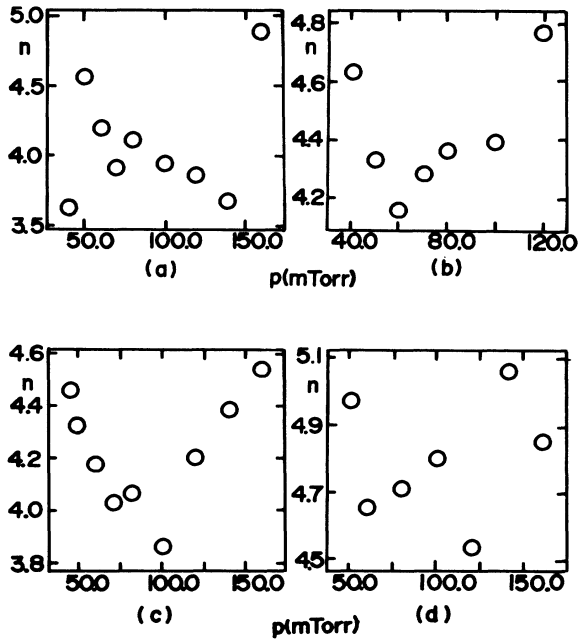

FIG. 26. Spectral indexes. Plots are given of spectral index n vs pressure (mTorr) for frequencies between 200 and 400 kHz. (a), (b), and (c) are for axial geometry with mixtures of 20%, 15%, and 10% CO_2. (d) is for azimuthal geometry for 15% CO_2.

in Ar. These slopes were obtained by a least-squares method for the case where $\ln(p)$ versus $\ln(f)$ is assumed. In Fig. 25 one sees that n decreases with an increase of pressure in varying amounts depending on the concentration of SF_6. Figure 26, where CO_2 is the gas additive, shows n to be small in the low-pressure region and large

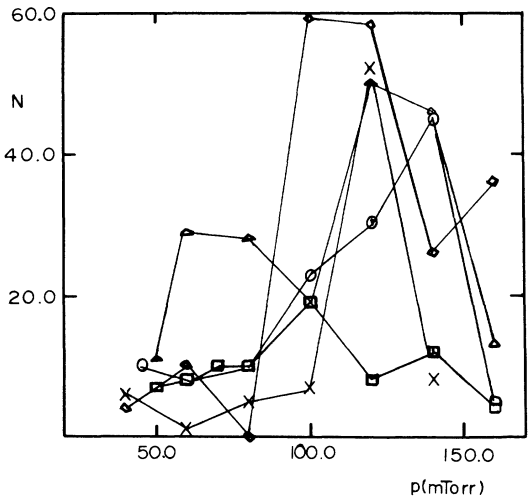

FIG. 27. Bispectral analysis: azimuthal case for SF_6. Plot of the number of peaks (N) in the bispectrum function $B(I,J)$ vs the mixture pressure (mTorr). Shown are those peaks for which $B(I,J)>0.45$. □ is for pure argon; ○ is for 5% mixture; △ is for 10% mixture; × is for 15% mixture; ◇ is for 20% mixture.

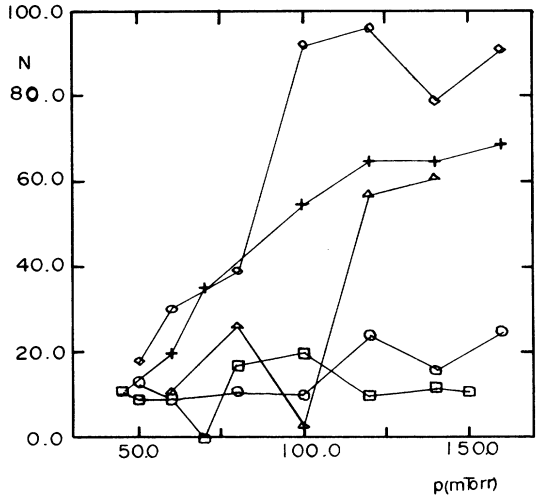

FIG. 28. Bispectral analysis: axial case for SF_6. Plot of N vs mixture pressure (mTorr). Shown are those peaks for which $B(I,J)>0.45$. □ is for pure argon; ○ is for 5% mixture; △ is for 10% mixture; × is for 15% mixture; ◇ is for 20% mixture.

in the high-pressure region.

Turbulent plasma theories[66,67] predict that the power spectra should fall off as ω^{-n}, n being the spectral index; experiments have found, generally, that $1<n<7$. Furthermore, the systematic decrease in n for various pressures and gas concentrations agrees well with previous autopower, cross-power and phase spectra.

Figures 27–30 are the plots of the number of peaks N in the bispectrum versus the mixture pressure for Ar and SF_6 and CO_2 for both the axial and azimuthal geometries. The bispectrum $B(I,J)$ is displayed only for those values where $B(I,J)>0.45$.

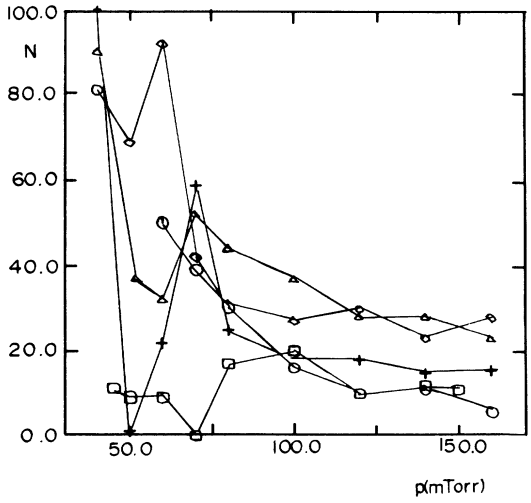

FIG. 29. Bispectral analysis: axial case for CO_2. Plot of N vs mixture pressure (mTorr). Shown are those peaks for which $B(I,J)>0.45$. □ is for pure argon; ○ is for 5% mixture; △ is for 10% mixture; × is for 15% mixture; ◇ is for 20% mixture.

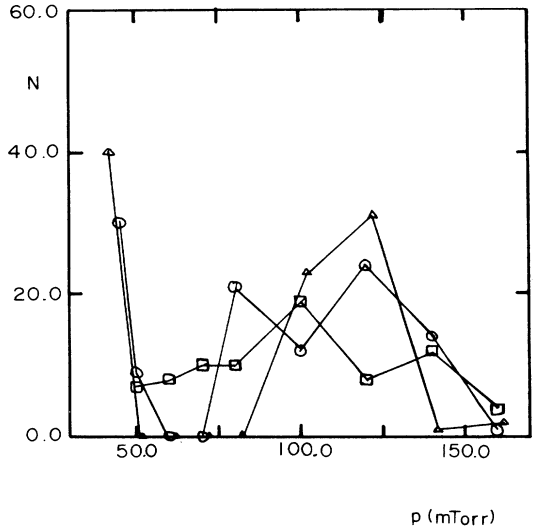

FIG. 30. Bispectral analysis: azimuthal case for CO_2. Plot of N vs mixture pressure (mTorr). Shwon are those peaks for which $B(I,J)>0.45$. □ is for pure argon; ○ is for 5% mixture; △ is for 10% mixture; × is for 15% mixture; ◇ is for 20% mixture.

Figure 27 shows results for the azimuthal geometry and various concentrations of SF_6. As may be seen, the number of peaks, N, first increases with an increase in pressure and gas concentration, but decreases in all cases at high pressures. The bispectrum data for the case of pure Ar is shown also for comparison. Figure 28 is the plot for axial geometry with SF_6 as the additive. Here N increases with pressure and concentration but there is no decrease in N as in the previous case.

The corresponding data for CO_2 are shown in Figs. 29 and 30. It is seen that N generally decreases with increasing pressure here. However, in Fig. 33 several cases of distinct maxima can be seen in N. The difference in behavior noticeable here, between CO_2 and SF_6, and Sec. IV A 2 (on spectral indexes) will be discussed in Sec. V.

In addition, we have found overall that $B(I,J)$ and the coupling coefficient $\mathcal{C}(I,J)$ are usually large for high-frequency couplings. Generally the contribution to the spontaneously excited modes of the system from the nonlinear wave-wave interaction is found in these data to lie between 25% and 40%.

V. DISCUSSION

A. Autopower and cross-power spectral analysis

The results of Sec. IV show that for both the axial and azimuthal probe configurations, when SF_6 is the additive in the discharge, the number of high-frequency modes increases with increases in concentration of SF_6 at a given pressure. Furthermore, at a given concentration, the number of high-frequency modes increases with pressure. This is reflected in the autopower and cross-power spec-

trum for the axial configuration. The autopower and cross-power spectra for the azimuthal case, while in general supporting the results for the axial case, differ from the axial case at high pressures. Here, in almost all cases, there is a decrease in the number of high-frequency modes at around 160 mTorr. This indicates that the azimuthal damping coefficient is more sensitive to pressure variation than its axial component. Thus waves traveling in the azimuthal plane from one probe to the other become attenuated at higher pressures and consequently, a smaller autopower and cross-power spectrum is obtained.

When CO_2 is the source of negative ions in the discharge an approximately inverse phenomenon takes place. It is at low pressures (40–70 mTorr) that the number of high-frequency components increases with increases in concentration of CO_2 at a given pressure. At high pressures (160 mTorr), only the dominant modes of the system survive and practically all high-frequency components are absent.

The fluctuation spectrum of a turbulent system tends towards the continuous as more and more degrees of freedom are excited. The autopower and cross-power spectra indicate that as the concentration of SF_6 and CO_2 is increased, a larger variety of oscillations are excited in the system. Thus the system becomes increasingly unstable as the concentration of negative ions is increased. As the concentration of negative ions increases, for a given initial fraction with pressure for SF_6, the system becomes more unstable at higher pressures. For CO_2 the negative-ion concentration decreases with pressure increase; hence maximum instability is seen only at low pressures.

B. Phase spectrum analysis

The phase spectrum analysis of Sec. IV, which gives the dispersion relation for the system, is useful in indicating the regions where the system departs from linearity. When SF_6 is the additive in the system, it is generally true that as the concentration of SF_6 is increased for a given pressure or as the pressure is increased for a given concentration, the dispersion curve deviates more from a straight line. In the azimuthal case, however, linearity is obtained at high pressure. When CO_2 is the additive, the nonlinear behavior manifests itself at low pressures, and the dispersion curve becomes linear at high pressures. The same, to a lesser degree, is true for the azimuthal case.

These results are very consistent with those of the previous paragraphs. The increasing instability of the system under the stated conditions causes the observed results. Furthermore, the phase spectra show the qualitative features which are to be expected when nonlinear wave-wave interactions are present.

C. Cross-correlation and spectral indexes analysis

The cross-correlation analysis of Sec. IV clearly shows that higher harmonics of the dominant mode are produced by increasing the concentration of negative ions. As the pressure is increased for a given concentration, the correlation time decreases. Furthermore, the dominant mode breaks up into several components at the higher pressures. When CO_2 is the additive, this breakup occurs at lower pressures than was the case for SF_6. At higher pressures, the mode is virtually unchanged. Thus as the concentration of negative ions increases, higher harmonics of modes occur in both cases—suggesting that the system is more turbulent under these conditions.

The spectral indexes n shown in Figs. 25 and 26, illustrate the shift of power from low-frequency to high-frequency modes. For SF_6, there is a general trend towards lower values of n at high pressures. The opposite occurs with CO_2. This clearly illustrated that more modes are being generated at higher frequencies under these conditions. For turbulent fluids the power spectra changes as w^{-n}, where the allowed range $1<n<7$ for plasmas is observed. As n decreases, the power in a given mode at higher frequencies increases. Thus the trend in n in our data indicates that the system is more turbulent at larger concentrations of negative ions.

D. Bispectral analysis

The bispectrum, as discussed before, is a direct quantitative indication of whether or not wave-wave interactions in the plasma have occurred.[2,54] It follows then that N, the number of significant peaks in the bispectrum, is a measure of how many such interactions have taken place. As a system becomes more turbulent, such a wave-wave interaction occurs with increasing frequency. Thus N may be used as a measure of the disturbance to the system by an instability.

Figures 27–30 illustrate the variation of N with pressure and concentration of SF_6 and CO_2 for the axial and azimuthal geometries. The general trend for SF_6 is that, as the concentration of SF_6 is increased for a given pressure, N increases. For a given pressure, N increases for all pressures shown for the axial case and decreases at high pressures for the azimuthal case. This trend was seen also in the autopower and cross-power spectra. These results therefore show that, in the azimuthal plane, the system becomes less turbulent at high pressures. In the axial direction, however, the system becomes more turbulent. When CO_2 is the additive, there is a general tendency for N to decrease as the pressure is increased, as shown in Figs. 29 and 30. At low pressures (40–75 mTorr), N is large and, for the axial case, shows prominent peaks at some concentrations. The general trend of these plots can be favorable compared with the corresponding autopower and cross-power spectra. The results thereby imply that when CO_2 is the source of negative ions, the system is more turbulent at low pressures than at high pressures.

We have determined the values of $B(I,J)$ and $\mathcal{C}(I,J)$, as defined in Sec. III, such that the modes I, J are actual peaks in the power spectrum of the system for a given set of firing conditions. We produce the sum and difference peaks in the power spectra where

$$(\text{sum})\, f_K = f_I + f_J \ ,$$

$$(\text{difference})\, f_K = f_I - f_J \ .$$

If either the sum or difference peaks do not exist in the power spectra, then the mode is represented as such by

0.0. With these procedures the bispectra $B(I,J)$ and $\mathcal{C}(I,J)$ are found to be large for those cases when (a) a low-frequency peak (I) couples with a high-frequency peak (J), or (b) both I and J are high-frequency modes of the system.

These behaviors may be understood if we define the power at mode K as due to two parts

$$P(K)=E(|X_K'|^2)+|\mathcal{C}(I,J)|^2E(|X_IX_J|^2)^2 .$$

The first part on the right-hand side is the contribution to $P(K)$ due to the spontaneous excitation of the mode f_K and the second term is the contribution to $P(K)$ due to the wave-wave interaction. In a turbulent environment, low-frequency modes of the system can couple with other modes, via the wave-wave interaction, to give rise to beat modes. It is reasonable then to expect that high-frequency modes which have a low probability of spontaneous generation, if present at all, will be in large part due to the three-wave interaction. Hence from the above equations, $B(I,J)$ and $\mathcal{C}(I,J)$ will be large for these couplings.

The procedures above also produced estimates of the amount of turbulent power present in a mode (which was shown to have some nonlinear component) due to spontaneous generation, i.e., arising through some mechanisms other than mode-mode coupling. Thus we can identify the modes where $B(I,J)$ and $\mathcal{C}(I,J)$ are relatively large, indicating that three-wave interactions play a considerable role and have a relatively greater contribution to the power $P(K)$. Consequently, we are able to determine that $P(K)$ receives a relatively small contribution from spontaneous (i.e., non-mode-mode) generation.

E. Overview

In the system under consideration, we of course expect ambipolar diffusion to play a central role in the transport of electrons and ions. Due to this diffusion, the radial electron concentration is given by

$$N_r=N_0J_0(2.405r/R) , \tag{4}$$

where R is the radius of the tube, N_0 is the density at $r\rightarrow 0$. The ambipolar electric field is given by

$$E_r=(kT_e/e)(1/N_r)(dN_r/dr) . \tag{5}$$

The ionization rate is

$$Z=\frac{mp}{e}\frac{4}{\sqrt{\pi}}\left[\frac{2kT}{m^{e-}}\right]^{3/2} \times\{[1+(eV_i/2kT_e)]\exp(-eV_i/kT_e)\} , \tag{6}$$

$$Z=A(T_e)e^{-eV_i/kT_e} .$$

Z is strongly dependent on the electron temperature. In the presence of negative ions, the diffusion theory is modified. The ambipolar field is now given by

$$\frac{E(\alpha)}{E(\varphi)}=\frac{1-D^+Da}{1+\alpha}\frac{(1+\gamma)}{\gamma} , \tag{7}$$

where

$$\alpha=\frac{N}{N_e};\quad \gamma=\frac{T_e}{T_+}=\frac{T_e}{T_-} .$$

Equation (7) has been experimentally verified for our system (see Fig. 6). A consequence of Eq. (6) is that the electron temperature follows the Schottky profile, which has been verified [Fig. 5(d)]. On that basis, it may be concluded that Eqs. (4)–(6) are valid for the range of operating conditions of our system.

When there are no negative ions in the system, Eq. (4) describes the distribution of the electrons. There are more electrons near the wall than at the core of the plasma column. The ambipolar field set up by this distribution, Eq. (5), gives rise to a Coulomb barrier which inhibits further transfer of electrons to the walls. If negative ions are now introduced into the system, the ambipolar field and consequently the Coulomb barrier decrease. This allows more electrons to leave the core, further increasing the core concentration of positive ions.

Figure 7(a) indicates that as the concentration of negative ions increases, so does the axial electric field. Most of the current in the discharge is carried by the electrons whose mobility is much greater than that for the ions. When the core is partially depleted of electrons, the axial field goes up in this region to maintain the same current. The increase in electric field, in turn, raises the electron temperature locally causing a large increase in Z [Eq. (3)]. Consequently, more electrons and ions are produced in the core. Those electrons capable of overcoming the Coulomb barrier escape to the walls. The low-energy electrons which cannot do so are left in the core where they may attach to SF_6 molecules to produce more negative ions.

Thus a positive feedback mechanism is established locally which gives rise to large local concentrations of positive ions in the core. The core is then susceptible to instability. Grabec has shown via computer simulation that the instabilities most common to noble gas discharges should arise as a result of the nonlinear dependence on the electron temperature of the ionization rate Z. Following his nomenclature [because Eq. (3) plays a central role in our model and in his analyses] this type of instability in our data may be called an ionization instability.

A qualitative explanation of the pressure dependence of the various autopower, cross-power spectra, and the bispectrum may be obtained by considering the well-known attachment cross sections.[21,41] We notice that the peak cross section for production of negative ions from SF_6 is 10^3 times larger than for CO_2. The peak in the attachment for SF_6 occurs at 0.1 or 0.25 eV and for CO_2, it occurs at 4.3 or 8.1 eV. Because the electron temperature follows the Schottky profile, the electron temperature decreases with an increase in pressure and increases with a decrease in pressure. At pressures of around 160 mTorr, from Fig. 5(d), then $T\simeq 0.5$ eV. Assuming that the electron distribution is Maxwellian, a large number of electrons will be available with energies in the range of 0.1–0.2 eV. Hence a large number of SF_6 molecules will attach electrons to form negative ions at these pressures.

It may be further noted that argon is transparent to electrons with energies of 0.2 eV due to the Ramsauer effect. Thus negative ions will be formed at most pressures, but will be significantly formed at higher pressures. At lower pressures, around 50 mTorr, we see from Fig. 5(c) that $T \simeq 2$ eV. Again, the Maxwellian distribution allows several electrons to be in the 3–5 eV range, giving rise to negative ions with CO_2.

Referring to Fig. 29, the peaks in the N versus p curves for some concentrations may be understood now and the model just outlined furnishes a qualitative explanation for some of our new results. However, it does not account for the difference at high pressures between the results for the axial and azimuthal geometries. To do this, a more refined theory would clearly be required.

VI. CONCLUSIONS

These are the first detailed quantitative analyses of the ion-density fluctuations in the positive column of a glow discharge containing a mixture of argon and two electron-attaching species, sulfur hexafluoride and carbon dioxide. We have found the following.

(1) The use of a probe biased in the orbital-limited region has allowed a determination of the negative-ion concentration (Fig. 6) for a steady-state discharge.

(2) The power spectrum of this fluctuation follows $P(w) \propto w^{-n}$ where $3 < n < 5$ (Figs. 25 and 26).

(3) The fluctuations in ion density are found to be three dimensional. The autopower spectra indicate that components of these fluctuations exist in the azimuthal and axial planes. The system consists of rotational and longitudinal oscillations with similar mode structures in each plane.

(4) A pronounced difference between the azimuthal and axial damping of fluctuations has been found. The azimuthal damping coefficient increases with pressure while the axial damping coefficient remains roughly insensitive to pressure change.

(5) The role of the negative ion in determining the stability of the system has been ascertained. An increase in the concentration of electron-attaching species increases the instability of the system at a given pressure. Furthermore, for a fixed concentration of electron-attaching species the instability of the discharges increases (decreases) with increase (decrease) of pressure, the direction of change depending entirely on the nature of the species involved.

(6) Nonlinear interactions play a very significant role in the evolution of fluctuation spectra to a multimode condition. The bispectrum is a valid and useful tool in the characterization of such interactions because (a) it has identified nonlinearly coupled modes, and (b) it has determined the coupling coefficient for these interactions.

(7) The concentration of the electron-attaching species and the total gas pressure are analogous to the parameter R in conventional hydrodynamics, and may be used to characterize the instability. The resulting physical model explains most of the phenomena which we have observed and it has, therefore, precise implications for other electron-attaching species, notably N_2O, NO, O_2, and CO, which have the same range of electron-attachment energy requirements as SF_6 and CO_2.

ACKNOWLEDGMENTS

This work was supported in part by U. S. National Aeronautics and Space Administration Grant No. NAG-1-377 and by U. S. Department of Energy Contract No. DE-AC02-83ER13041. Some of this work was submitted by Raghu Ramaiah of the Graduate Faculty of Rutgers University in partial fulfillment of the requirements for the Ph.D. degree in Physics.

[1]R. N. Franklin, *Plasma Phenomena in Gas Discharges* (Clarendon, Oxford, 1976), pp. 20–38, 81–112, 138–183.
[2]F. F. Cap, *Handbook on Plasma Instabilities* (Academic, New York, 1976), Vol. 1, pp. 35–51, 251–351.
[3]A. B. Stewart, J. Phys. D, **27**, 911 (1956).
[4]W. L. Nighan, W. J. Weigan, and R. A. Hass, Appl. Phys. Lett. **22**, 579 (1973).
[5]T. Donahue and G. H. Dieke, Phys. Rev. **81**, 248 (1951).
[6]A. V. Nedopasov and Yu. B. Ponomarenko, High Temp. (USSR) **3**, 12 (1965).
[7]M. Yamada and M. Raether, Phys. Fluids **18**, 361 (1975).
[8]D. B. Ilic, Phys. Fluids **20**, 1717 (1975).
[9]M. Tanibayashi, J. Phys. Soc. Jpn. **30**, 1188 (1971).
[10]A. J. Anastassiades, and E. Sideris, J. Appl. Phys. **51**, 5675 (1980).
[11]M. Porkolab and R. P. H. Chang, Rev. Mod. Phys. **50**, 745 (1978).
[12]R. C. Davidson, *Methods in Non-linear Plasma Theory,* (Academic, New York, 1971), pp. 1–15, 133–151, 274–315.
[13]W. L. Nighan and W. J. Weigan, Phys. Rev. A **10**, 922 (1974).
[14]G. Francis, in *Encyclopedia of Physics,* edited by S. Flugge (Springer-Verlag, New York, 1956), Vol. XXII, pp. 53–203.
[15]K. G. Emelius, E. W. Gray, J. R. M. Coulter, and G. A. Woolsey, Int. J. Electron., **25**, 367 (1968).
[16]I. Ishikawa, and S. Sugamomata, J. Appl. Phys. **15**, 1855 (1976).
[17]S. Sugamomata, I. Ishikawa, H. Yamagushi, and M. Matsumato, Phys. Lett. **78A**, 71 (1980).
[18]J. B. Thomson, Proc. R. Soc. London **73**, 818 (1959).
[19]M. V. Koninkov, Zh. Eksp. Teor. Fiz. **7**, 908 (1958) [Sov. Phys.—JETP **34**, 629 (1958)].
[20]G. A. Woolsey, K. G. Emelius, E. W. Gray, and J. R. M. Coultler, Int. J. Electron. **22**, 235 (1967).
[21]H. Massey, *Negative Ions* (Cambridge University Press, Cambridge, 1976), pp. 23, 345–376.
[22]E. Nasser, *Fundamentals of Gaseous Ionization and Plasma Electronics* (Wiley, New York, 1971), pp. 80, 399, 414–420.
[23]S. C. Brown, *Introduction to Electrical Discharges in Gases,* (Wiley, New York, 1966), pp. 215–223.
[24]Yu. B. Golubovsdii, Yu. M. Kagan, and R. I. Lyagushchenko, Opt. Spectrosc. **25**, 79 (1968).
[25]B. B. Kadomtsev, *Plasma Turbulence,* (Academic, New York, 1965), pp. 1–65.
[26]L. D. Landau, and E. M. Lifshitz, *Fluid Mechanics* (Addison-

Wesley, Reading, Mass., 1959), pp. 102–145.
[27]N. D'Angelo, Phys. Fluids **10**, 719 (1967).
[28]J. R. Roth, Phys. Fluids **10**, 2712 (1967).
[29]O. Kofoed-Hansen, Phys. Fluids **12**, 2124 (1969).
[30]R. A. Haas, Phys. Rev. **8**, 1017 (1973).
[31]A. I. Akhiezer, I. A. Akhiezer, and V. V. Angeleiko, Zh. Eksp. Teor. Fiz. **57**, 870 (1969) [Sov. Phys.—JETP **30**, 476, (1970)].
[32]I. Grabec, Phys. Fluids **17**, 10 (1974).
[33]L. L. Lengyl, Phys. Lett. **29A**, 60 (1969).
[34]I. Grabec and S. Mikac, Plasma Phys. **16**, 1155 (1974).
[35]L. Pekarek, Usp. Fiz. Nauk **94**, 132 (1968) [Sov. Phys.—Usp. **11**, 188 (1968)].
[36]A. V. Nedopasov, Sov. Phys. Usp. **11**, 174 (1968).
[37]A. V. Nedopasov, Sov. Phys. Tech. Phys., **3**, 153 (1958).
[38]N. L. Oleson and A. W. Cooper, Adv. Electron. Electron Phys. **24**, 155 (1968).
[39]P. S. Landa, N. A. Miskinova, and Yu. V. Ponomarev, Usp. Fiziol. Nauk. **132**, 601 (1980) [Sov. Phys. Usp. **23**, 813 (1980)].
[40]I. M. Chapnik, J. Phys. D **14**, 121 (1981).
[41]D. Rapp and D. D. Brigwa, J. Chem. Phys. **43**, 1480 (1965).
[42]W. M. Hickam and R. W. Fox, J. Chem. Phys. **25**, 642 (1956).
[43]F. J. Mehr and M. A. Biondi, Phys. Rev. **181**, 246 (1969).
[44]J. N. Bardsley, J. Phys. B **1**, 365 (1968).
[45]E. W. McDaniel, *Collisional Phenomena in Ionized Gases* (Wiley, New York, 1964), pp. 405, 410–420.
[46]R. K. Asundi, J. D. Craggs, and M. V. Kurepa, Proc. Phys. Soc. London **82**, 967 (1963).
[47]F. C. Fehsenfeld, J. Chem. Phys. **53**, 2000 (1970).
[48]A. Chutijian, Phys. Rev. Lett. **46**, 1511 (1981).
[49]K. F. Shoenberg, Rev. Sci. Instrum. **51**, 1151 (1980).
[50]J. A. Blackburn, *Spectral Analysis: Methods and Techniques,* (Marcel Dekker Inc., New York, 1970), pp. 28–31, 55, 56, 141.
[51]E. O. Brigham, *Fast Fourier Transform* (Prentice Hall, Englewood Cliffs, New Jersey, 1974), pp. 83, 209–219.
[52]D. E. Smith, E. J. Powers, and G. S. Caldwell, IEEE Trans. Plasma Sci. **PS-2**, 261 (1974).
[53]Y. C. Kim, E. J. Powers, IEEE Trans. Plasma Sci. **PS-7**, 120 (1979).
[54]Y. C. Kim, J. M. Bell, and E. J. Powers, Phys. Fluids **23**, 253 (1980).
[55]J. F. Kaiser and W. A. Reed, Rev. Sci. Instrum. **48**, 1447 (1977).
[56]Y. C. Kim, L. Khadra, and E. J. Powers, Phys. Fluids **23**, 2250 (1980).
[57]K. H. Geissler, R. A. Greenwald, and W. Calvert, Phys. Fluids **15**, 96 (1972).
[58]A. J. Ahearn and N. B. Hannay, J. Chem. Phys. **21**, 119 (1953).
[59]S. Wantabe, J. Plasma Phys. **14**, 353 (1975).
[60]K. L. Wong and J. R. Wilson, Phys. Fluids **23**, 96 (1980).
[61]R. S. Powers, J. Appl. Phys. **37**, 3821 (1966).
[62]K. J. Harker and D. B. Illic, Rev. Sci. Instrum. **45**, 1315 (1974).
[63]E. B. Hooper, Jr., Plasma Phys. **13**, 1 (1971).
[64]F. F. Chen, in *Plasma Diagnostic Techniques,* edited by R. H. Huddlestone and S. L. Leonard (Academic, New York, 1965) pp. 113–201.
[65]R. P. Smy, Adv. Phys. **5**, 517 (1976).
[66]J. R. Roth, Phys. Fluids **14**, 2193 (1971).
[67]D. E. Smith and E. J. Powers, Phys. Fluids, **16**, 1373, (1972).
[68]D. Smith, A. G. Dearn, and N. G. Adams, J. Phys. D **7**, 1944 (1974).
[69]C. V. Goodall and D. Smith, Plasma Phys. **10**, 249 (1968).
[70]D. Smith, C. V. Goodall, N. G. Adams, and A. G. Dean, J. Phys. D **5**, 1226 (1972).
[71]D. Smith and I. C. Plumb, J. Phys. D **3**, 34 (1970).
[72]D. Smith and I. C. Plumb, J. Phys. D **6**, 196 (1973).
[73]T. J. M. Boyd and J. J. Sanderson, *Plasma Dynamics* (Barnes & Noble, New York, 1969), pp. 1–58.
[74]L. S. B. Kovasnay, in *Structure and Mechanism in Turbulence,* edited by H. Fielder (Springer-Verlag, New York, 1978), Vol. I, pp 1–18.
[75]J. A. Johnson III, R. Ramaiah, and Lin I, in *International Union of Theoretical and Applied Mechanics Symposium on Unsteady Turbulent Shear Flows,* edited by F. Shroeder (Springer-Verlag, Berlin, 1981), pp. 318–329.
[76]J. A. Johnson III, R. Ramaiah, and J. Santiago, Rev. Sci. Instrum. **52**, 936 (1981).